

1 **Upper Atmosphere Responses to the 2022 Hunga Tonga-Hunga Ha’apai**

2 **Volcanic Eruption via Acoustic-Gravity Waves and Air-Sea Interaction**

3 Qinzeng Li<sup>1,5</sup>, Jiyao Xu<sup>1,2\*</sup>, Aditya Riadi Gusman<sup>3</sup>, Hanli Liu<sup>4</sup>, Wei Yuan<sup>1,5</sup>, Weijun Liu<sup>1,5</sup>,  
4 Yajun Zhu<sup>1,5</sup>, and Xiao Liu<sup>6</sup>

5

6 1. State Key Laboratory of Space Weather, National Space Science Center, Chinese Academy of Sciences,  
7 Beijing, 100190, China

8 2. School of Astronomy and Space Science, University of Chinese Academy of Science, Beijing,  
9 100049, China

10 3. GNS Science, Lower Hutt, New Zealand

11 4. High Altitude Observatory, National Center for Atmospheric Research, Boulder, Colorado, USA

12 5. Hainan National Field Science Observation and Research Observatory for Space Weather, National Space  
13 Science Center, Chinese Academy of Sciences, Beijing, 100190, China

14 6. School of Mathematics and Information Science, Henan Normal University, Xinxiang, China

15

16 Corresponding author: Jiyao Xu (jyxu@swl.ac.cn)

17 **Abstract**

18 Multi-group of strong atmospheric waves (wave packets #1-#5) over China associated  
19 with the 2022 Hunga Tonga–Hunga Ha’apai (HTHH) volcano eruptions were observed in the  
20 mesopause region using a ground-based airglow imager network. The horizontal phase speed  
21 of wave packet #1 and #2 is approximately 309 m/s and 236 m/s respectively, which is  
22 consistent with Lamb wave L0 mode and L1 mode from theoretical prediction. The amplitude  
23 of the lamb wave L1 mode is larger than that of L0 mode. The wave fronts of Lamb wave L0  
24 and L1 below the lower thermosphere are vertical, while the wave fronts of L0 mode tilt  
25 forward above exhibiting internal wave characteristics, which show good agreement with the  
26 theoretical results. Two types of tsunamis were simulated, one type of tsunami is induced by  
27 the atmospheric pressure wave (TIAPW) and the other type tsunami is directly induced by the  
28 Tonga volcano eruption (TITVE). From backward ray tracing analysis, the TIAPW and  
29 TITVE were likely the sources of the wave packet #3 and wave packets #4-5, respectively.  
30 The scale of tsunamis near the coast is very consistent with the atmospheric AGWs observed  
31 by the airglow network. The AGWs triggered by TITVE propagate nearly 3000 km inland  
32 with the support of duct. The atmospheric pressure wave can directly affect the upper  
33 atmosphere, and can also be coupled with the upper atmosphere through the indirect way of  
34 generating tsunami and subsequently tsunami generating AGWs, which will provide a new  
35 understanding of the coupling between ocean and atmosphere.

## 36 **1. Introduction**

37 Hunga Tonga–Hunga Ha’apai (HTHH) volcano, which erupted at 04:14:45 UT on  
38 January 15, 2022, produced the largest volcanic eruption in terms of energy release of a  
39 single event since the Krakatoa volcanic eruption (Symons, 1888) in 1883. This volcanic  
40 eruption triggered broad spectrum atmospheric disturbances (Adam, 2022; Duncombe,  
41 2022; Wright et al., 2022), including Lamb waves (Zhang et al., 2022), acoustic waves,  
42 gravity waves (GWs) (Liu et al., 2022), and shock waves (Astafyeva et al., 2022). In  
43 addition, the travelling ionospheric disturbances (TIDs) caused by this volcanic eruption  
44 have also been reported (Themens et al., 2022; Lin et al., 2022).

45 Lamb waves are external wave propagating along Earth’s surface at the speed of  
46 sound (Beer, 1974). They are non-dispersive or nearly non-dispersive (Francis, 1973) and  
47 can propagate horizontally over long distances. Lamb wave mainly occupies the  
48 troposphere, and its perturbation pressure decays exponentially with height (Yeh and Liu,  
49 1974). The Lamb waves excited by the Tonga volcano eruptions went around the Earth  
50 several times (Amores et al., 2022; Duncombe, 2022). Sepúlveda et al. (2023) found that  
51 the wind field strongly affects the morphology and propagation of Lamb wave. Liu et al.  
52 (2023) reproduced the Lamb wave L0 and L1 modes consistently with theoretical  
53 predictions (Francis, 1973) using high-resolution Whole Atmosphere Community Climate  
54 Model with thermosphere/ionosphere extension (WACCM-X). Li et al. (2023) identified  
55 Lamb wave L1 mode using phase-leveling amplitude technology based on global  
56 navigation satellite system (GNSS)- total electron content (TEC). Poblet et al. (2023)  
57 reported that the strong perturbations in the horizontal wind field is caused by lamb wave

58 L1 mode associated with the 2022 HTHH volcano eruption.

59 Acoustic-gravity waves (AGWs) are mechanical waves in compressible fluids in a  
60 gravity field (Gossard and Hooke, 1975). If the frequencies are much larger than the  
61 buoyancy frequency, AGWs tend towards acoustic wave mode, and when the frequency is  
62 much smaller than the buoyancy frequency, the fluid can be considered incompressible, and  
63 the AGWs tend towards internal GWs mode. The term “acoustic-gravity waves” is usually  
64 used when restoring forces due to both gravity and compressibility are important. AGWs  
65 are known to play a significant role in the coupling between the atmosphere/ionosphere and  
66 the ocean (Press and Harkrider, 1962; Harkrider and Press, 1967; Donn and Balachandran,  
67 1981; Azeem et al., 2017). Atmospheric pressure waves are mechanical waves that are  
68 related to the density of the atmosphere. Compression and expansion are the high-pressure  
69 and low-pressure regions of motion in a medium.

70 The 2022 HTHH volcano eruption triggered tsunamis that affected the whole world  
71 (Carvajal et al., 2022; Ghent et al., 2022). Conventional tsunamis are typically generated by  
72 localized sea surface displacements caused by sources such as earthquakes and volcanoes,  
73 similar to the tsunamis directly induced by the 2022 Tonga volcano eruption (TITVE).  
74 Another tsunami is induced by the atmospheric pressure wave (TIAPW) (Kubota et al.,  
75 2022; Gusman et al., 2022). Tsunami can generate upward propagating AGWs through  
76 water-air interface and propagate to the thermosphere/ionosphere (Hines, 1972; Peltier and  
77 Hines, 1976; Hickey et al., 2009, 2010; Occhippinti et al., 2013; Vadas et al., 2015;  
78 Laughman et al., 2016; Nishikawa et al., 2023; Pradipta et al., 2023). Using the red line  
79 airglow imager, Makela et al. (2011) detected airglow disturbance in Hawaii that arrived

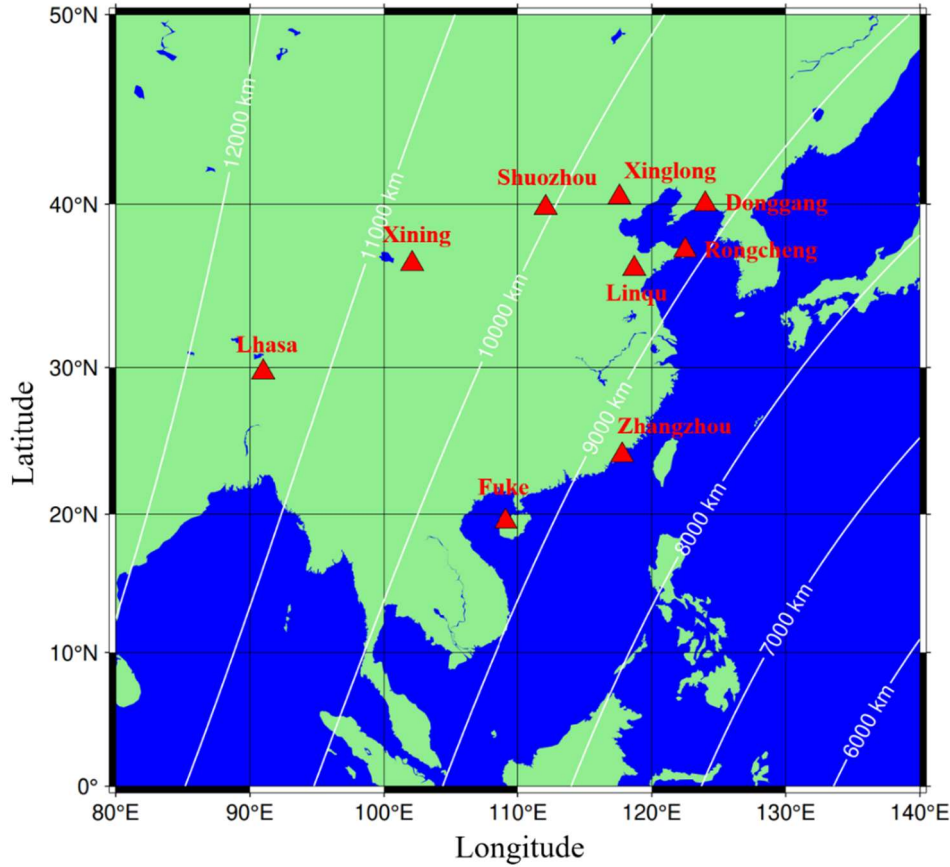
80 1hr earlier of the tsunami generated by the 11 March 2011 Tohoku earthquake. Also using  
81 the redline airglow, Smith et al. (2015) observed tsunami and GW almost simultaneously in  
82 Chile. Inchin et al. (2020) used a three dimensional (3D) numerical model to simulate the  
83 atmospheric AGWs generated by tsunami. They found that bathymetry variations  
84 significantly affected the tsunamis and the AGWs excited by tsunamis, leading to their  
85 nonlinear evolution process. More recently, Inchin et al. (2022) performed the numerical  
86 simulations of mesopause airglow radiation fluctuations induced by tsunami-generated  
87 AGWs, and found that large-scale tsunamis can cause detectable and quantitative  
88 disturbances of mesopause airglow through AGWs.

89 As far as we know, the research on the impact of tsunamis induced atmospheric  
90 AGWs on the atmosphere and ionosphere shown above is all caused by conventional  
91 tsunami. There are only two rare studies on the ground-based airglow observations of  
92 AGWs caused by this conventional tsunami, and both are limited to red line observations  
93 (Makela et al., 2011; Smith et al., 2015). However, the observation of tsunami induced  
94 AGWs in the mesopause region observed by ground-based airglow imaging has never been  
95 reported. In this study, we first reported the propagation characteristics of the AGWs  
96 generated by the tsunamis triggered by the 2022 HTHH volcano eruptions in the  
97 mesopause region using the ground-based airglow imager observation network. We then  
98 focus on the coupling process of atmospheric pressure waves triggering tsunamis, and then  
99 tsunamis generating atmospheric AGWs through air-water-air-coupling process in the  
100 far-field area of the 2022 HTHH volcano eruption.

## 101 **2. Data and Methods**

## 102 **2.1 Multi layer airglow imager network**

103 A multi-layer airglow observation network (Xu et al., 2021) was built to study  
104 atmospheric disturbances excited by severe weather events, such as thunderstorms (Xu et  
105 al., 2015), typhoons (Li et al., 2022) and volcanic activities. Figure 1 shows the distribution  
106 of the multi-layer airglow observation network station. The multi-layer airglow observation  
107 network mainly includes the OH airglow network, which has been used to observe the  
108 airglow layer at the height of 87 km; the OI airglow network has been used to observe the  
109 airglow layer at the height of 250 km. In addition, there were 557 nm airglow and Na  
110 airglow imagers installed at some stations, such as Xinglong Station (40.4°N, 117.6°E). The  
111 airglow network can provide observation with high temporal and spatial resolution. The  
112 temporal resolution is 1 min and the spatial resolution is 1 km. The time resolution of OH  
113 and 557 nm airglow imager is 1 minute, while the resolution of OI airglow is 2 minutes.  
114 The spatial resolution of the airglow imager at the airglow layer is not uniform. The  
115 resolutions of OH, OI 557 nm, and OI 630 nm airglow in the zenith direction are 0.27 km,  
116 0.29 km, and 0.77 km, respectively, while in the zenith angle of 60°, the resolutions are  
117 1.01 km (OH), 1.11 km (OI 557 nm), and 2.65 km (OI 630 nm), respectively.

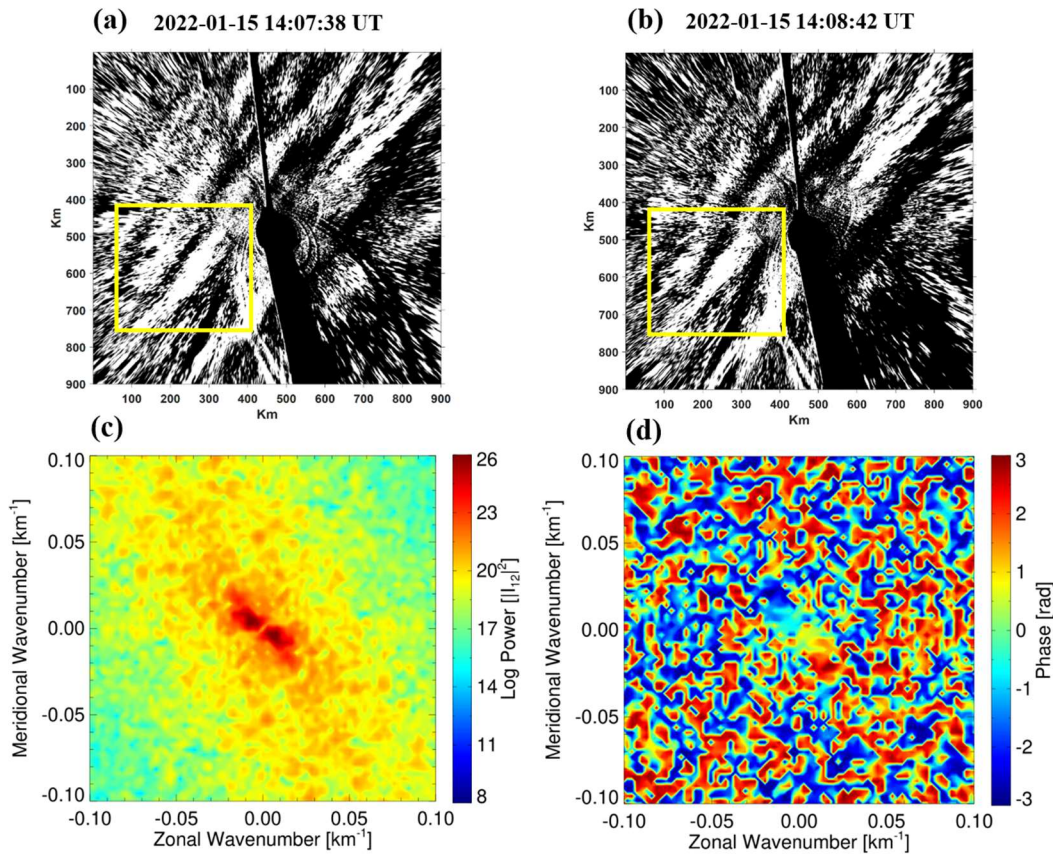


118  
 119 **Figure 1** The distribution of airglow network stations, along with the large circular  
 120 centered on the Tonga volcano and its radius length, is also marked in the figure

121 **2.2 Spectral analysis of atmospheric wave parameters**

122 The airglow image was calibrated with the help of standard star map (Garcia et al.,  
 123 1997) and projected into geospatial space. The background radiation is removed by time  
 124 differential (TD) method (Swenson and Mende, 1994), to highlight atmospheric  
 125 fluctuations. The atmospheric wave parameters (horizontal wavelength  $\lambda_h$ , observed  
 126 horizontal phase speed  $c$ , and the relative intensity perturbation  $I'/I$ ) are extracted from  
 127 spectral analysis method. Figure 2c presents the two-dimensional cross spectrum obtained  
 128 from Fig. 2a and 2b. Zonal ( $k_x$ ) and meridional ( $k_y$ ) wave numbers are determined from  
 129 the peak position of the spectra. The horizontal wavelengths  $\lambda_h$  are obtained from the  
 130 expression of  $\lambda_h = 2\pi / \sqrt{k_x^2 + k_y^2}$ . The observed speeds  $c$  are calculated from the phase ( $\varphi$ )

131 (Fig. 2d) at the maximum peak of the cross spectrum as  $c = \frac{\varphi}{2\pi} \frac{\lambda_h}{\Delta t}$ , where  $\Delta t$  is the time  
 132 interval between the two TD images. The amplitudes of intensity perturbations were  
 133 calculated by integrating the power surrounding the central peaks of the power spectrum.  
 134 To eliminate noise, the energy of the wave spectrum should be greater than 10% of the total  
 135 spectrum (Tang et al., 2005).



136  
 137 **Figure 2** The time difference images (a-b) obtained from the Xinglong OH airglow imager on the night  
 138 of 15 February 2022. Each image is projected on an area of 250 km × 250 km. The (c) cross spectrum  
 139 and (d) phase of the time difference images from a and b using 2-D fast Fourier transform.

### 140 2.3 Tsunami simulation model

141 Tonga submarine volcano erupted on 15 January 2022, and generated tsunamis that  
 142 were detected around the globe, affected particularly the Pacific region. In this study, two  
 143 types of tsunamis were simulated, conventional tsunami simulations and atmospheric  
 144 pressure wave-induced tsunami simulations. The linear-shallow water equations in the



145 spherical coordinate system are used to simulate the tsunamis from the localized source and  
 146 atmospheric pressure wave. The continuity equation of a linear shallow water wave model  
 147 in spherical coordinates is:

$$148 \quad \frac{\partial \eta}{\partial t} + \frac{1}{R \sin \theta} \left[ \frac{\partial(ud)}{\partial \varphi} + \sin \theta \frac{\partial(vd)}{\partial \theta} \right] = 0 \quad (1)$$

149 where  $\eta$  is free surface elevation (m),  $d$  is the water depth (m),  $R$  is the Earth's  
 150 radius (6371,000 m),  $\varphi$  is longitude,  $\theta$  is colatitude.

151 While the momentum equations of the linear shallow water wave model are:

$$152 \quad \frac{\partial u}{\partial t} + \frac{1}{R \sin \theta} \left[ g \frac{\partial \eta}{\partial \varphi} + \frac{1}{\rho} \frac{\partial p}{\partial \varphi} \right] + fv = 0 \quad (2)$$

$$153 \quad \frac{\partial v}{\partial t} + \frac{1}{R} \left[ g \frac{\partial \eta}{\partial \theta} + \frac{1}{\rho} \frac{\partial p}{\partial \theta} \right] - fu = 0 \quad (3)$$

154 where,  $u$  is the velocity along the lines of longitude (m/s),  $v$  is the velocity along  
 155 the lines of latitude,  $g$  is the gravitational acceleration ( $9.81 \text{ m/s}^2$ ),  $p$  is the  
 156 atmospheric pressure (Pa),  $\rho$  is the sea water density ( $1026 \text{ kg/m}^3$ ),  $f$  is the Coriolis  
 157 coefficient. For the atmospheric pressure wave-induced tsunami simulation, the moving  
 158 change pressure terms as an input to tsunami simulation momentum equation. The  
 159 atmospheric pressure wave model is based on the Equation (1) in Gusman et al. (2022).

160 For the tsunami simulations from a localized source, a B-spline function (Koketsu and  
 161 Higashi, 1992) below is used to represent the circular water uplift source at the volcano:

$$162 \quad f(x, y) = \sum_{i=0}^3 \sum_{j=0}^3 c_{k+i, l+j} B_{4-i} \left( \frac{x-x_k}{h} \right) B_{4-j} \left( \frac{y-y_l}{h} \right) \quad (4)$$

163 where  $B_i(r) = \begin{cases} r^3/6, & i=1 \\ (-3r^3 + 3r^2 + 3r + 1)/6, & i=2 \\ (3r^3 - 6r^2 + 4)/6, & i=3 \\ (-r^3 + 3r^2 - 3r + 1)/6, & i=4 \end{cases}$  (5)

164  $x_k$  and  $x_l$  stand for the coordinates of the knots along the x and y axes, h is the  
 165 characteristic diameter of water uplift,  $r$  is the great-circle distance from the volcano  
 166 eruption center,  $c_{1,1} = 1$  and the other  $c_{k+i,l+j} = 0$ . In this study, the modelling domain covers  
 167 the Pacific Ocean and some parts of Indian Ocean and the Caribbean with a grid size of 5  
 168 arc-min. For detailed tsunami simulation algorithms, please refer to Gusman et al. (2022).  
 169 The models for the 2022 HTHH volcanic eruption used in this study was estimated and  
 170 validated with observations at offshore DART stations around the Pacific Ocean in a  
 171 previous study (Fig. 3 and Fig. 7 of Gusman et al., 2022).

## 172 2.4 Ray tracing method

173 The following ray tracing equations (Lighthill, 1978) describes the propagation path of  
 174 AGWs.

175 
$$\frac{dx_i}{dt} = \frac{\partial \omega}{\partial k_i} = c_{g_i}$$
 (6)

176 
$$\frac{dk_i}{dt} = -\frac{\partial \omega}{\partial x_i}$$
 (7)

177 where  $x_i$ ,  $k_i$ ,  $c_{g_i}$  ( $i=1, 2, 3$ ), and  $\omega$  are the position vector, wavenumber vector,  
 178 group speed, and intrinsic frequency, respectively.

179 Using the dispersion relation of acoustic gravity wave (Yeh and Liu, 1974), we can  
 180 assess the vertical propagation state of AGWs. The dispersion relation is as follows

181 
$$m^2 = \frac{\omega^2}{c_s^2} \left(1 - \frac{\omega_a^2}{\omega^2}\right) - k^2 \left(1 - \frac{\omega_b^2}{\omega^2}\right)$$
 (8)

182 where  $m$  is the vertical wave number,  $k$  is the horizontal wave number,  $c_s$  the local speed of  
183 sound,  $\omega = k(c - u)$  is intrinsic frequency,  $u$  is the background wind speed in the direction of  
184 wave propagation from meteor radar observations and ERA-5 (Hersbach et al., 2020).

185  $\omega_a^2 = \frac{g}{T} \frac{dT}{dz} + \frac{\gamma g}{4H}$  is acoustic cutoff frequency,  $\omega_b^2 = \frac{g}{T} \frac{dT}{dz} + \frac{(\gamma - 1)g}{\gamma H}$  is buoyancy frequency,

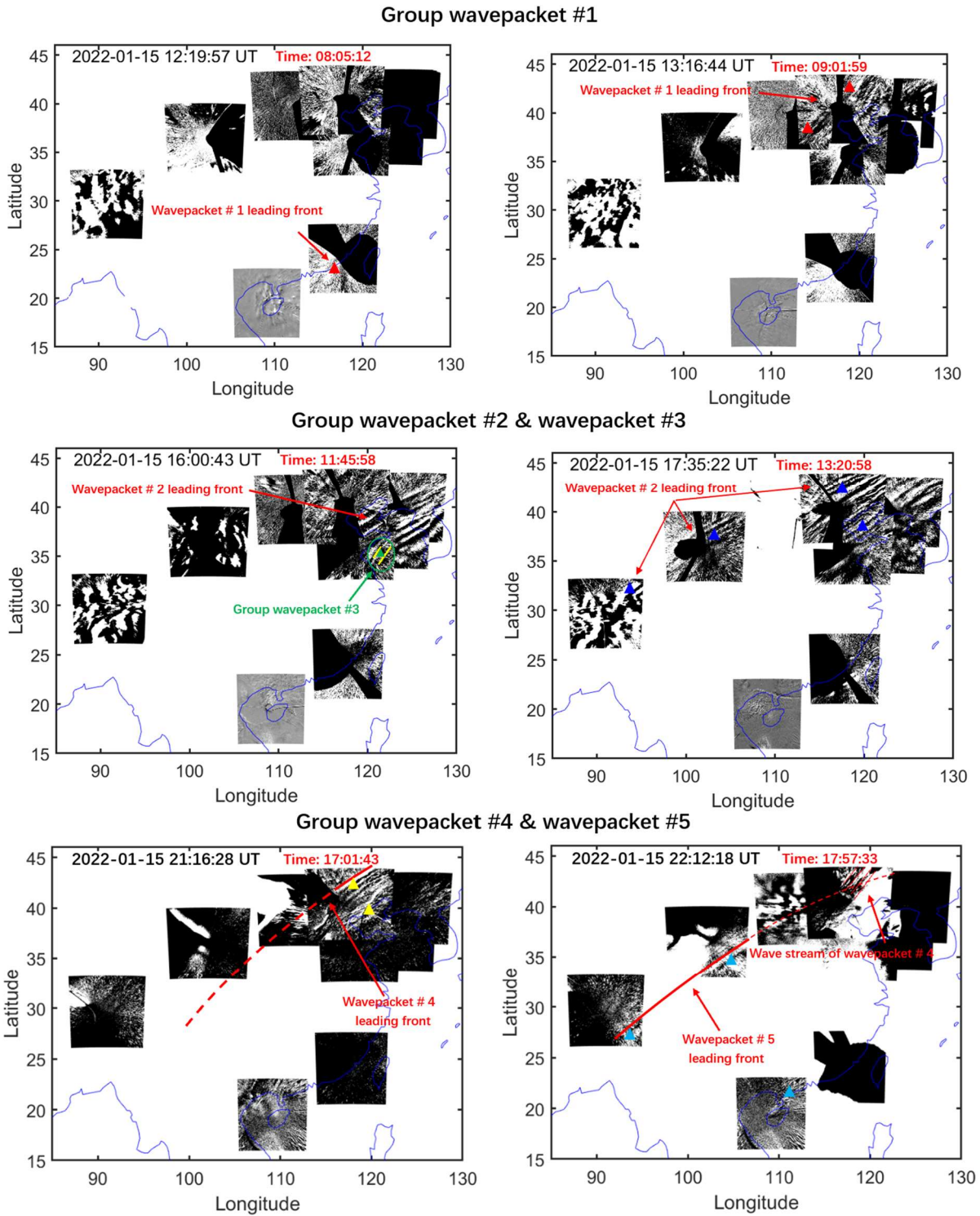
186  $g$  is the gravitational acceleration, and  $T$  is temperature from the Sounding of the  
187 Atmosphere using Broad band Emission Radiometry (SABER) instrument on the  
188 Thermosphere Ionosphere Mesosphere Energetics and Dynamics (TIMED) satellite. When  
189  $\omega > \omega_a$  or  $\omega < \omega_b$ ,  $m^2 > 0$ , AGW can propagate freely, while when  $\omega_b < \omega < \omega_a$ ,  $m^2 < 0$ , the wave is  
190 evanescent.

### 191 **3. Results and Discussion**

#### 192 **3.1 Upper Atmospheric Airglow Responses to HTHH Volcanic Eruption via Lamb** 193 **Waves**

194 Five groups of atmospheric waves (wave packets #1-5) were observed in the  
195 mesopause region by the ground-based airglow network. Refer to this Supplement  
196 (<https://doi.org/10.5446/66190>) for detailed wave propagation status. To eliminate random  
197 disturbances, we also made videos of two days before and after the volcanic eruption  
198 (<https://av.tib.eu/series/1689>). From the videos, it can be seen that the OH airglow layer  
199 was very calm during this period. Figure 3 shows the wave packet #1 observed by the  
200 airglow imager network (top panels). Wave packet #1 entered the view of the airglow  
201 network approximately 8 hr after the HTHH volcanic eruption (Left image of top panels).  
202 Three hours after wave packet #1 entered the field of view, wave packet #2 was observed  
203 by the airglow network. The leading front of wave packet #2 has an uninterrupted

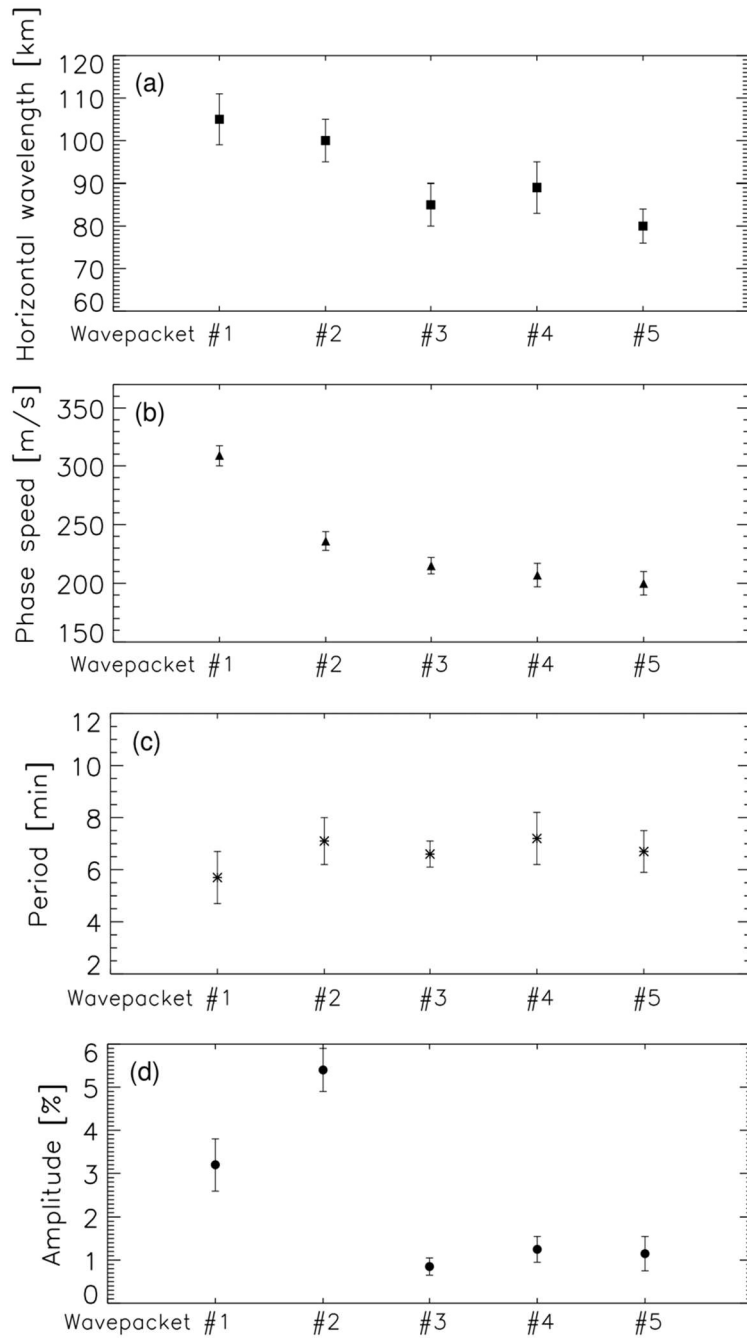
204 continuous front, which almost covers the whole Chinese Mainland (middle panels).  
205 Interestingly, we observed AGWs accompanying wave packet #2 (hereafter wave packet #3)  
206 over the northwest region of the Yellow Sea (Left image of middle panels). Wave packet #2  
207 always keeps a stable state in the process of propagation, and maintains a regular front  
208 when propagating over Lhasa Station (29.7°N, 91.0°E). Wave packet #4 exhibits strong  
209 instability characteristics during propagation. Compared to the continuous leading front of  
210 wave packet #2, the fronts of wave packets #4 and #5 are separated (bottom panels). We  
211 also found that wave packet #5 propagate more than 3000 km inland (propagating to the  
212 area west of longitude 90°E).



213  
 214 **Figure 3** Five strong group atmospheric waves associated with the Tonga volcano eruptions were  
 215 observed in the mesopause region by the ground-based airglow network. Different colored triangles  
 216 correspond to each wave event sampling point, while red, blue, green, yellow, and cyan correspond to  
 217 wavepackets #1, #2, #3, #4, and #5, respectively. The red time markers in this figure and the following  
 218 figure represent the lapse time since the volcano eruption.

219 Figure 4 shows the distribution of wave parameters for multi-group of atmospheric

220 waves (wave packets #1-#5) from cross spectral analysis. The phase speed of wave packet  
221 #1 is approximately 309 m/s. Wave packet #2 displays a slightly slower phase speed, with  
222 average phase speed of 236 m/s. The horizontal phase speeds of group wave packets # 3-5  
223 are mainly distributed in the range of 200 m/s to 215 m/s, which is smaller than that of  
224 wave packets # 1-2. The horizontal wavelengths of these five group wave packets are  
225 mainly distributed in 80 km-105 km, while the observation periods are relatively small and  
226 mainly concentrated in 5.7 min-7.2 min. For amplitude, the average amplitude of the lamb  
227 wave L1 mode (5.4%) is higher than that of the lamb wave L0 mode (3.2%). Wavepackets  
228 # 3, # 4, and # 5 have relatively small amplitudes, mainly distributed between 0.85% and  
229 1.25%.



230  
 231 **Figure 4** Distribution of (a) horizontal wave wavelength, (b) phase speed, (c) period, and (d) amplitude  
 232 parameters for multi-group of atmospheric waves (wave packets #1-#5). The calculation of wave packet  
 233 parameters comes from the average value of the wave passing through the sampling points in Fig 3.

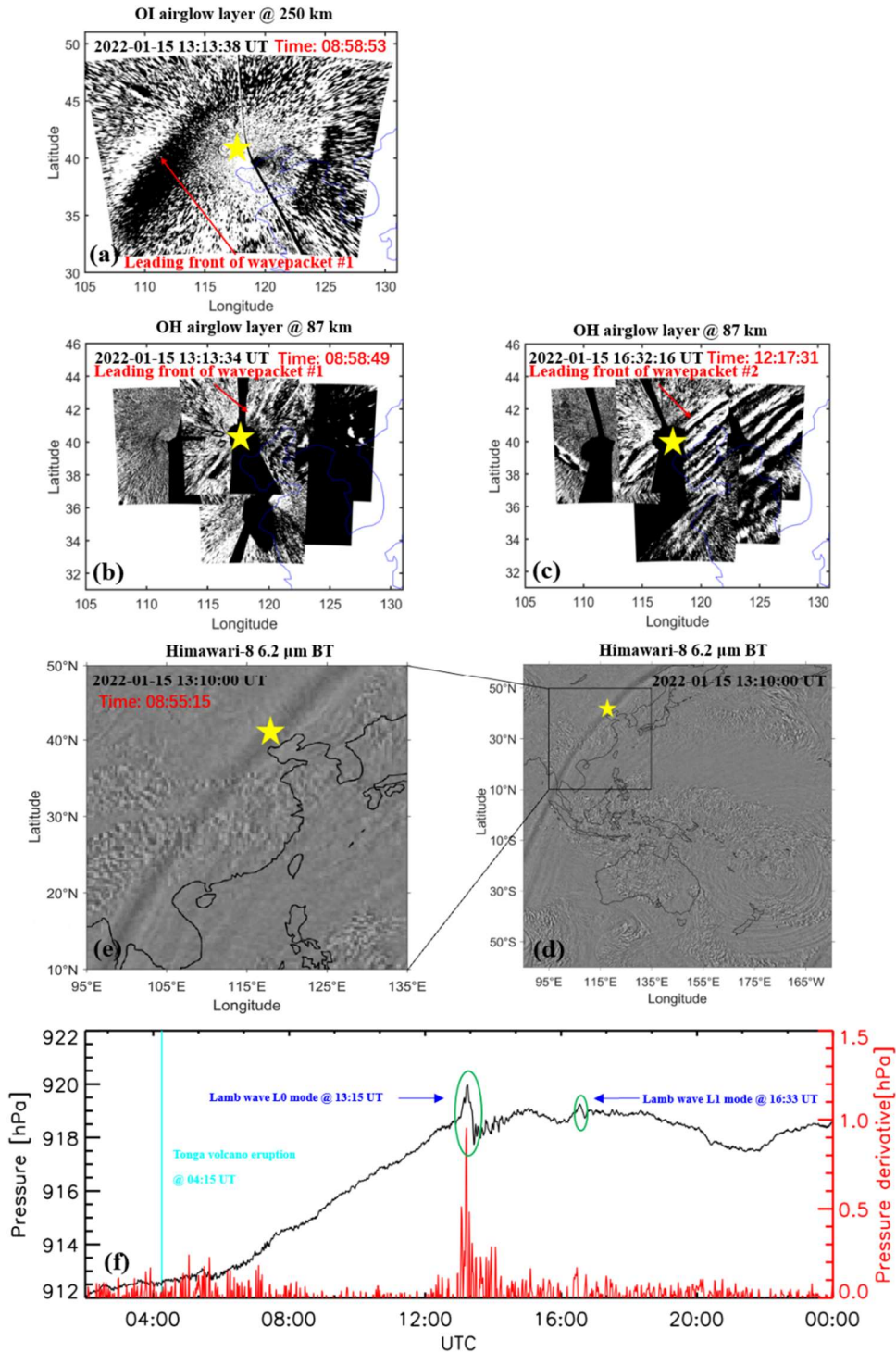
234 The HTHH volcano eruption produced Lamb waves that propagate around the globe,  
 235 (Wright et al., 2022) causing sudden changes in surface pressure (Omira et al, 2022;  
 236 Takahashi et al., 2023). Figure 5f shows the surface air pressure data of Xinglong station  
 237 (40.4°N, 117.6 °E). At 13:15 UT on January 15, 2022, the air pressure dropped sharply from

238 920 Pa to 917.7 Pa, indicating that Lamb wave arrived at the surface of Xinglong station at  
239 13:15 UT. A small disturbance of air pressure occurs at 16:33 UT. Figures 5e and 5d present  
240 Himawari-8 6.2  $\mu\text{m}$  brightness temperature at 13:10:00 UT (Otsuka, 2022). It can be seen  
241 that the leading front of Lamb wave L0 mode happens to pass through the zenith direction  
242 of Xinglong station. The time when wave packet #1 (Fig. 5b) and wave packet #2 (Fig. 5c)  
243 reach the zenith direction of Xinglong Station from OH airglow observation is 13:13:34 UT  
244 and 16:32:16 UT, which matches the time for surface pressure disturbances quite well. The  
245 phase speed of the wave packet #1 ( $\sim 309$  m/s) is very close to the speed of surface Lamb  
246 wave (L0 mode). From the Fig 5, it can be seen that the phase of the lamb wave L0 mode is  
247 almost vertical from the ground to the stratosphere and then to the mesosphere. The wave  
248 packet # 2 with a slower phase speed ( $\sim 236$  m/s) is consistent with the Lamb wave L1  
249 mode in theoretical predictions (Francis, 1973) and simulations from WACCM-X model  
250 (Liu et al., 2023). However, at almost the same time, the wave front observed in the  
251 thermosphere (Video Supplement, <https://doi.org/10.5446/66280>) with a slightly faster  
252 phase speed of 342 m/s is nearly 550 km a head of the wave front in the mesopause region  
253 in the horizontal propagation direction and ahead of time approximately 30 min (Fig. 5a).  
254 This is in good agreement with theoretical and modeling results (Fig. 4 of Lindzen and  
255 Blake, 1972; Fig. 2 of Liu et al. 2023), which show that the wave fronts of Lamb wave  
256 below the lower thermosphere are vertical and tilt forward above. As for Lamb wave L1  
257 mode, the ground and mesopause region provide waveguide surfaces, resulting in  
258 maximum wave energy between the two layer, while the phase does not change with height  
259 (Francis, 1973).



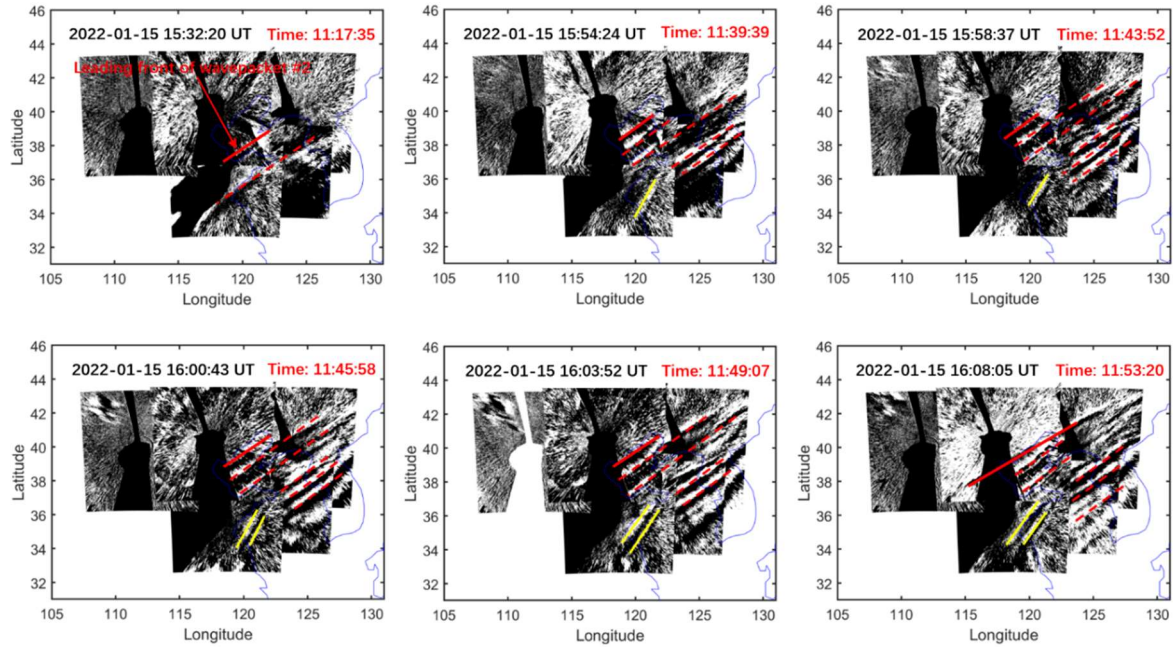
260 As for why the observed Lamb wave L0 shape in the OH airglow layer is not a strong  
261 leading wave with much weaker trailing waves, it may be caused by the following factors.  
262 It is seen from model simulations that the wave amplitudes of L0 and L1 modes are not  
263 uniform at the wave front. This non-uniformity becomes more pronounced in the upper  
264 atmosphere (e.g. Fig 2 of Liu et al., 2023), probably as a result of the large variation of the  
265 background atmosphere propagation conditions. It is thus possible that over certain regions  
266 the trailing waves become comparable with the leading wave. In addition, due to the  
267 smaller field of view of the airglow imager compared to satellite observations, some  
268 structures may be related to local fine structures, especially in the middle and upper layers  
269 where many internal waves have significant amplitudes, which may be relatively more  
270 significant than Lamb waves.

271 As mentioned above, the amplitude of Lamb wave L1 mode in the mesopause region  
272 is greater than that of L0 mode, which may be due to the fact that L1 mode is an internal  
273 wave below the mesopause (Liu et al. 2023). For an isothermal atmosphere, the Lamb wave  
274 L0 mode amplitude grows with altitude  $z$  as  $e^{\kappa z/H}$ , where  $H$  is the scale height,  $\kappa = (\gamma - 1)/\gamma$ ,  
275 and  $\gamma$  is the ratio of specific heats ( $\sim 1.4$ ). However, the amplitude of internal GWs varies as  
276  $e^{z/2H}$ . The amplitude of internal waves increases with height at a rate greater than that of  
277 surface modes.



278

279 **Figure 5** (a) OI 630 nm airglow observation at 13:13:18 UT. OH airglow network observations when (b)  
 280 wave packet #1 and (c) wave packet #2 pass through the zenith direction of Xinglong Station at 13:13:34  
 281 UT and at 16:32:16 UT, respectively. (d)-(e) Himawari-8 6.2 μm brightness temperature at 13:10:00 UT.  
 282 (f) The surface time series of surface pressure obtained from Xinglong observation station. The red line  
 283 represents the time derivative of the pressure. The sudden change of air pressure at 13:15 UT indicates  
 284 the arrival time of Lamb wave L0. A small disturbance of air pressure occurs at 16:33 UT indicates the  
 285 arrival time of Lamb wave L1. The yellow stars represent the location of the Xinglong station.



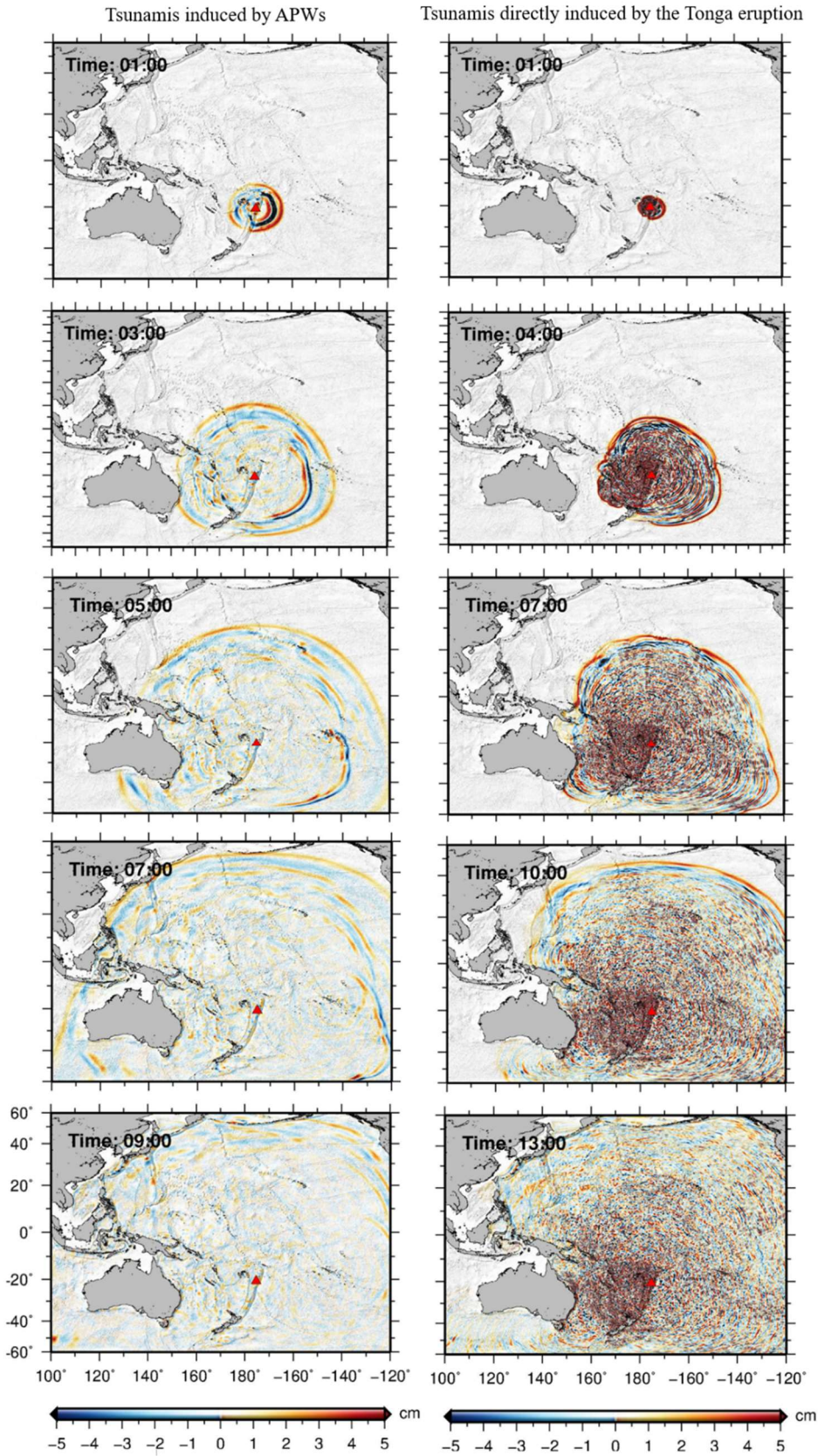
286  
 287 **Figure 6** The red solid lines indicate leading wave front of the wave packet #2. The yellow solid lines  
 288 mark wave packet #3, which are clearly not parallel to the wave fronts of wave packet #2.

289 Figure 6 shows the time sequence of propagation image of wave packet #3. We found  
 290 that with the propagation of wave packet #2, there is an AGW (wave packet #3) with a  
 291 certain angle between its phase plane (yellow solid line) and the phase plane of wave  
 292 packet #2. This implies that the source of the wave packet #3 is different from that of wave  
 293 packet #2. The horizontal wavelength of the wave packet #3 near the coast is  $84 \text{ km} \pm 5$   
 294 km.

### 295 **3.2 Simulation of Tsunami induced by HTHH Volcano Eruption**

296 The 2022 HTHH volcano eruption triggered global atmospheric pressure waves. The  
 297 simulated atmospheric pressure waves propagate at an approximate constant speed of 317  
 298 m/s, and the amplitude decreases with the distance from the volcano (Gusman et al., 2022).  
 299 Figure 7 shows snapshots of the TIAPW and TITVE simulation results. The leading  
 300 TIAPW excited by the pressure disturbances travels at the same speed as the atmospheric

301 pressure wave and is followed by subsequent sea waves generated earlier in the  
302 atmospheric pressure wave propagation which thereafter travel at the conventional tsunami  
303 propagation speed. Under a given pressure gradient, the discharge flux in deep sea is much  
304 greater than that in shallow water. A deep bathymetric feature such as the Kermadec Tonga  
305 Trench can more effectively generate tsunami waves. The wave train following the leading  
306 wave travelling over the trench appear to be larger than those travelling in other directions.  
307 The propagation speed of TITVE from the shallow water (long) wave approximation is  
308  $v = \sqrt{gH_0}$  (Salmon, 2014), where  $g$  is the gravitational acceleration and  $H_0$  is the ocean  
309 depth. For sea water with a general depth of 4 km, the speed of shallow water wave is about  
310 200 m/s. Therefore, the TIAPW is significantly faster than the TITVE. The amplitude of  
311 TITVE is greater than that of tsunamis generated by atmospheric pressure waves. The wave  
312 train following the leading wave of TITVE exhibit finer structures with scales smaller than  
313 that of TIAPW. We found that the TIAPW arrived along the coast of Chinese Mainland  
314 about 4-5 hours earlier than the TITVE.

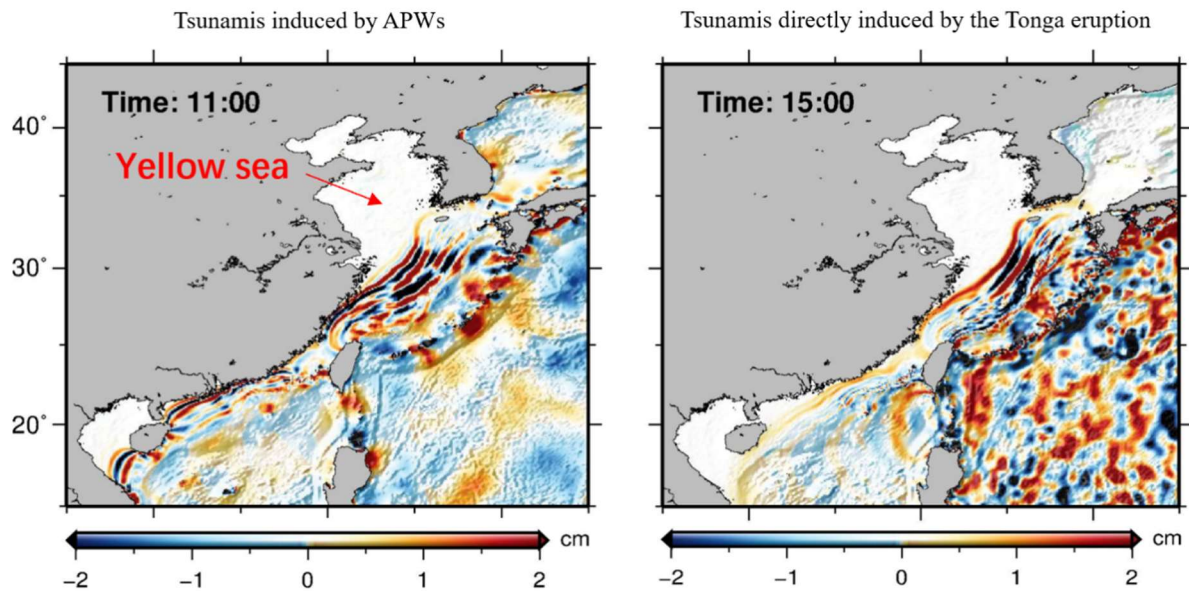


315  
 316 **Figure 7** Snapshots of simulated tsunamis induced by the atmospheric pressure wave (left panels) and  
 317 tsunamis directly induced by the Tonga volcano eruption (right panels).

### 318 **3.3 Upper atmosphere responses to HTHH volcanic eruption via Air-Sea Interaction**

319 Figure 8 shows the simulation results of TIAPW and TITVE near the coast of Chinese  
320 Mainland 11 hr (15:15 UT) and 15 hr (19:15 UT) after the volcanic eruption, respectively.  
321 Air pressure waves are not very efficient at directly exciting tsunamis in shallow water due  
322 to the weaker air-sea coupling (Gusman et al., 2022; Yamada et al., 2022). The Yellow sea  
323 is quite shallow, so the amplitude of the leading of TIAPW is very small there. The leading  
324 wave is followed by subsequent waves with larger amplitudes, which propagate in the  
325 same direction as the leading wave but at the conventional tsunami speed (Gusman et al.,  
326 2022). We found that the TIAPW and TITVE on the continental shelf have shorter  
327 wavelengths compared with those in the deep ocean. When the tsunamis approached the  
328 coast of China, three groups of AGWs (wave packet #3 and wave packets #4-5) were  
329 observed by the airglow network. The time when the AGW entered the view of the airglow  
330 network was very close to the time when the Tonga tsunamis reached the coast of Chinese  
331 Mainland. The wave packet #3 entered the airglow network at 15:30 UT and the wave  
332 packets #4-5 entered the airglow network at 19:40 UT. This strongly suggests that the wave  
333 packets detected by the airglow network are correlated to the tsunamis near the coast. We  
334 found that as the tsunamis approached the coast of China, they diffracted between Taiwan  
335 and Philippines and became discontinuous. And the wave packets #4 and #5 we observed  
336 was also discontinuous, which further confirms the correlation between wave packets # 4-5  
337 and discontinuous tsunamis. We estimate that the average wavelength of TIAPW near the  
338 coast of the Yellow Sea is approximately  $82 \text{ km} \pm 4 \text{ km}$ , which is very consistent with the  
339 horizontal wavelengths of the atmospheric AGW observed by airglow network as mention

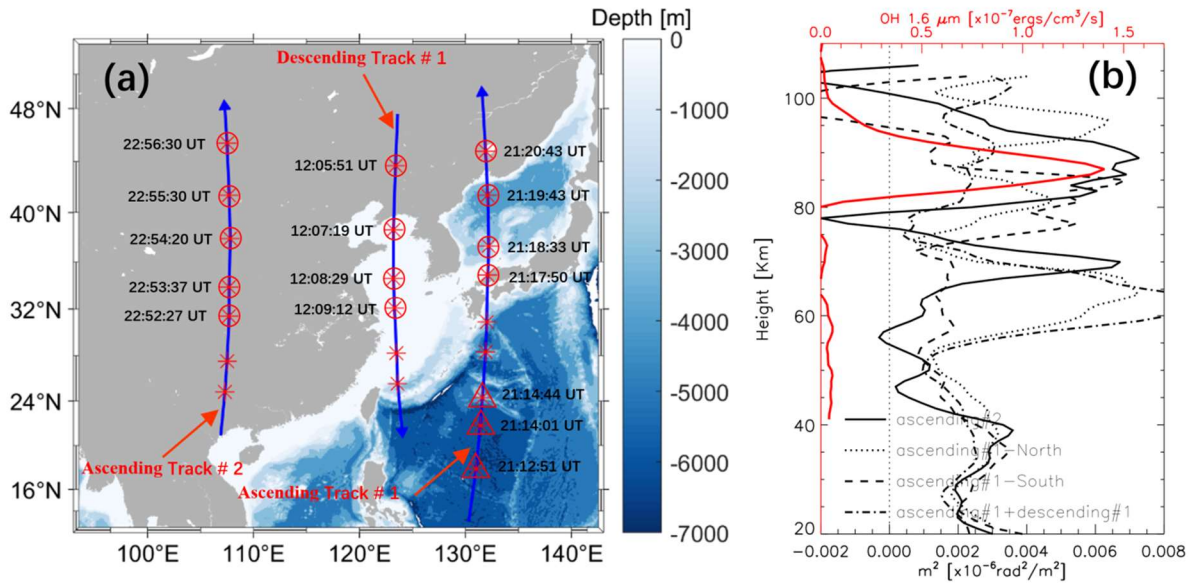
340 above ( $84 \text{ km} \pm 5 \text{ km}$ ), while the average wavelengths of TITVE near the coast of the  
 341 Yellow Sea and South Sea are  $95 \pm 5 \text{ km}$  and  $86 \pm 5 \text{ km}$ , respectively.



342  
 343 **Figure 8** Simulated tsunamis induced by the atmospheric pressure wave (left panels) and tsunamis  
 344 directly induced by the Tonga volcano eruption (right panels) near the coast of Chinese Mainland. The  
 345 marked time represents the time after the volcanic eruption.

346 Figure 9a shows three TIMED satellite tracks with descending track #1 along the coast  
 347 of China, ascending track #1 located east of the Korean Peninsula, and ascending track #2  
 348 inland China. Figure 9b shows the square of vertical wave number  $m^2$  profile (black)  
 349 derived from the average temperature from the limb viewing of the Sounding of the  
 350 Atmosphere using SABER/ TIMED measurement locations marked by the red circles and  
 351 triangles in Fig.9a. We take the average temperature of ascending track #1 and descending  
 352 track #1 serves as the background temperature for the wave packet #3 and ascending track  
 353 #1 as the background temperature of the wave packets #4-5 when they propagate in the  
 354 coastal vicinity. We take ascending track #2 as the background temperature of wave packets  
 355 #4-5 when they propagate inland China. The peak height of OH airglow layer is 87 km. We  
 356 found that the propagation of wave packet #3 (dash-dotted line) is in a state of free

357 propagation in the coastal vicinity.



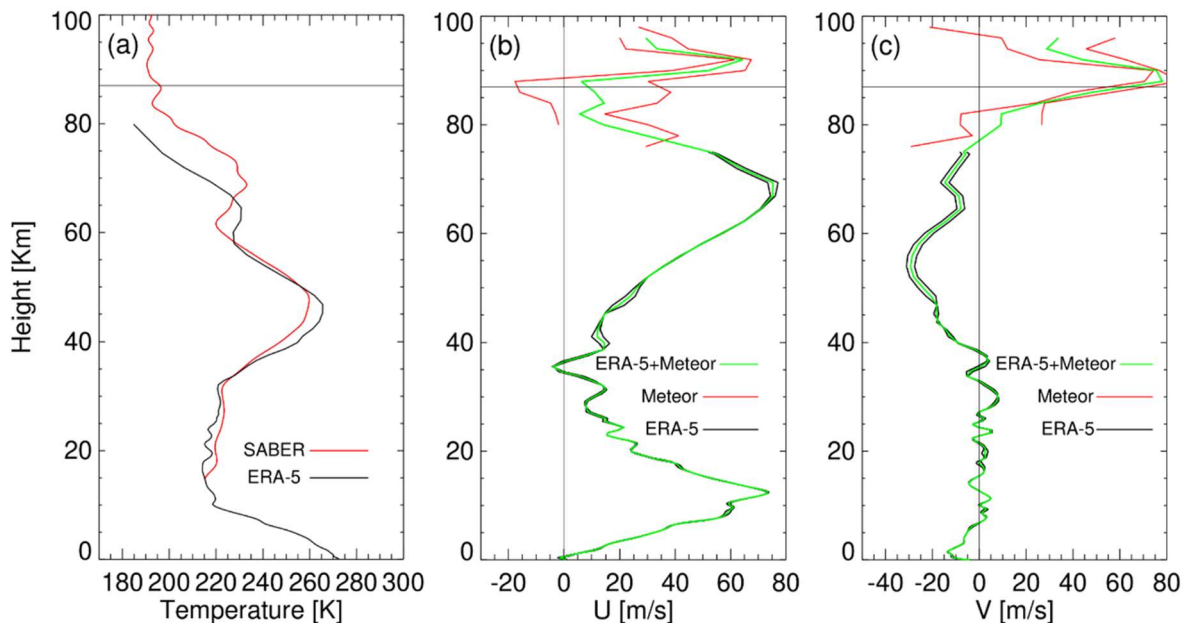
358  
 359 **Figure 9** (a) Ascending and descending SABER/TIMED satellite tracks over Chinese Mainland.  
 360 Background representative ocean depth map. (b) Square of vertical wave number  $m^2$  profiles: black solid  
 361 line profile derived from the ascending track #2 (marked by the red circle), dotted line profile derived  
 362 from the ascending track #1-North (marked by the red circle), dashed line profile derived from the  
 363 ascending track #1-South (marked by the red triangle), and dash-dotted line profile derived from the  
 364 average the ascending track #1 and descending track #1 (marked by the red circle) from the  
 365 SABER/TIMED measurement locations in (a). The red line represents the OH 1.6  $\mu\text{m}$  emission intensity  
 366 obtained by the SABER/TIMED.

367 Figure 10 show the background field used for ray tracing analysis for the TIAPW  
 368 event. The temperature comes from TIMED/SABER and ERA-5 and wind data from  
 369 meteor radar and ERA-5. Meteor radar wind field is from Beijing station (40.3°N, 116.2°E).  
 370 Figure 11 shows the results of ray tracing for the wave packet #3. We find that the source  
 371 location of AGWs over the coast of Chinese Mainland falls in the near coast where the  
 372 tsunami occurred.

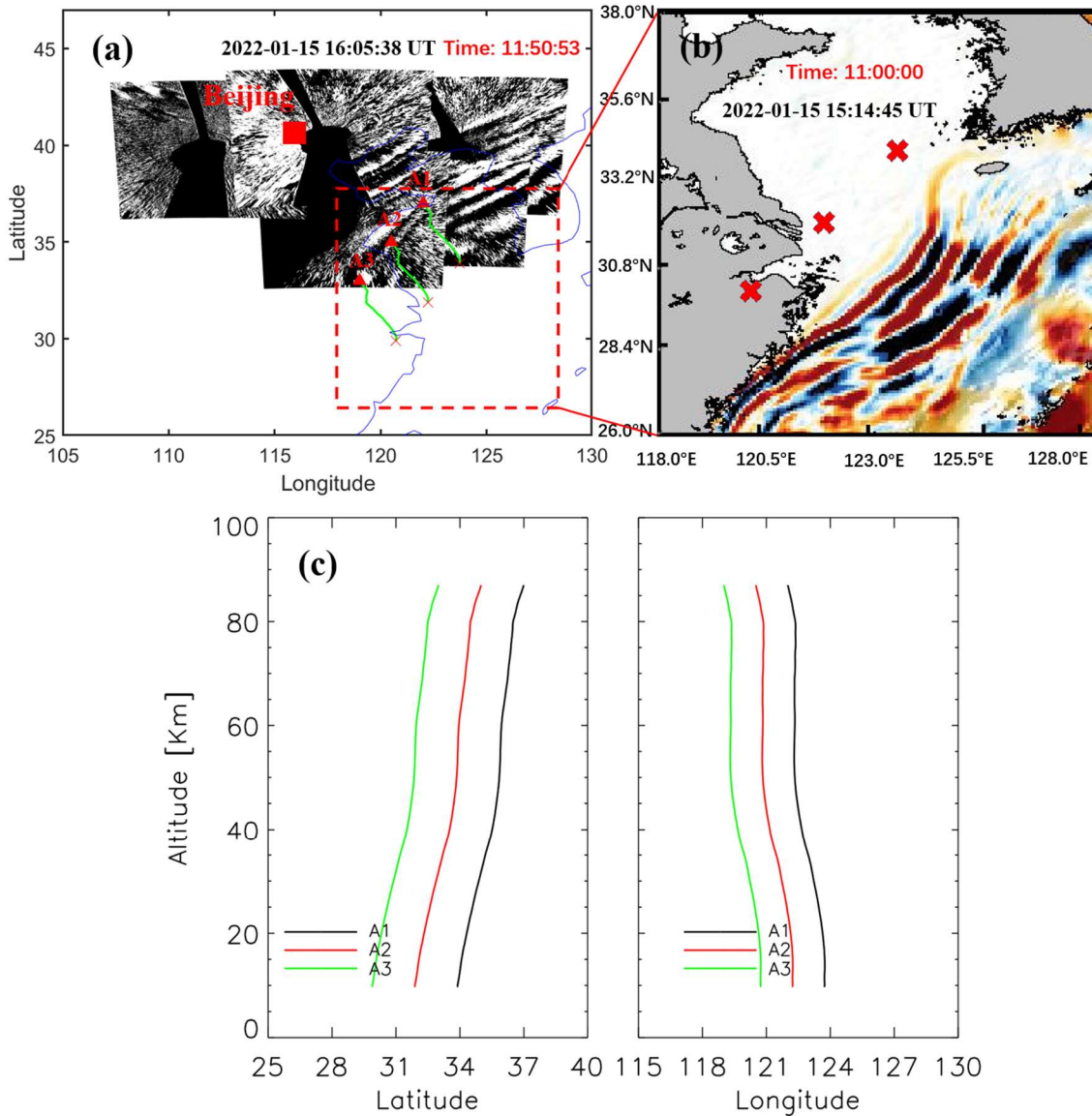
373 Tsunami simulation shows that the surface wave height along the coast of Chinese  
 374 Mainland is in the order of 2 cm. There have been theoretical (Peltier and Hines, 1976) and  
 375 observational (Grave and Makela, 2015, 2017) studies on the relationship between the



376 amplitude of tsunamis and GWs. Peltier and Hines (1976) found that a tsunami amplitude  
 377 of  $\pm 1$  cm at sea level can cause vertical motion of ionospheric E layer and F layer  $\pm 100$  m.  
 378 A more direct observational evidence is that Grawe and Makela (2017) provided airglow  
 379 observation of tsunami-generated ionospheric signatures over Hawaii caused by the 16  
 380 September 2015 Illapel earthquake. They found that vertical disturbances on the sea surface  
 381 not exceeding 2 cm (Fig. 3b of Grave and Makela, 2017) can create detectable signatures in  
 382 the ionosphere (Fig. 1 of Grave and Makela, 2017). Therefore, we suggest that the waves  
 383 with larger amplitudes following the leading of TIAPW interact with the atmosphere after  
 384 arriving at the coast of Chinese Mainland to generate the upward propagating AGW packet.



385  
 386 **Figure 10** The background field used for ray tracing analysis for the TIAPW event (a) Saber temperature  
 387 (red) comes from the average temperature of ascending track #1 and descending track #1 in Fig. 9, and  
 388 ERA-5 temperature (black) comes from the average of 15:00 UT and 16:00 UT. (b) Meteor zonal wind  
 389 field (red) and ERA-5 zonal wind field (black). (c) Meteor meridional wind field (red) and ERA-5  
 390 meridional wind field (black). The two red and black lines in (b) and (c) are respectively from 15:00 UT  
 391 and 16:00 UT. The green lines represent the average of two lines. Meteor radar wind field is from  
 392 Beijing station.  
 393



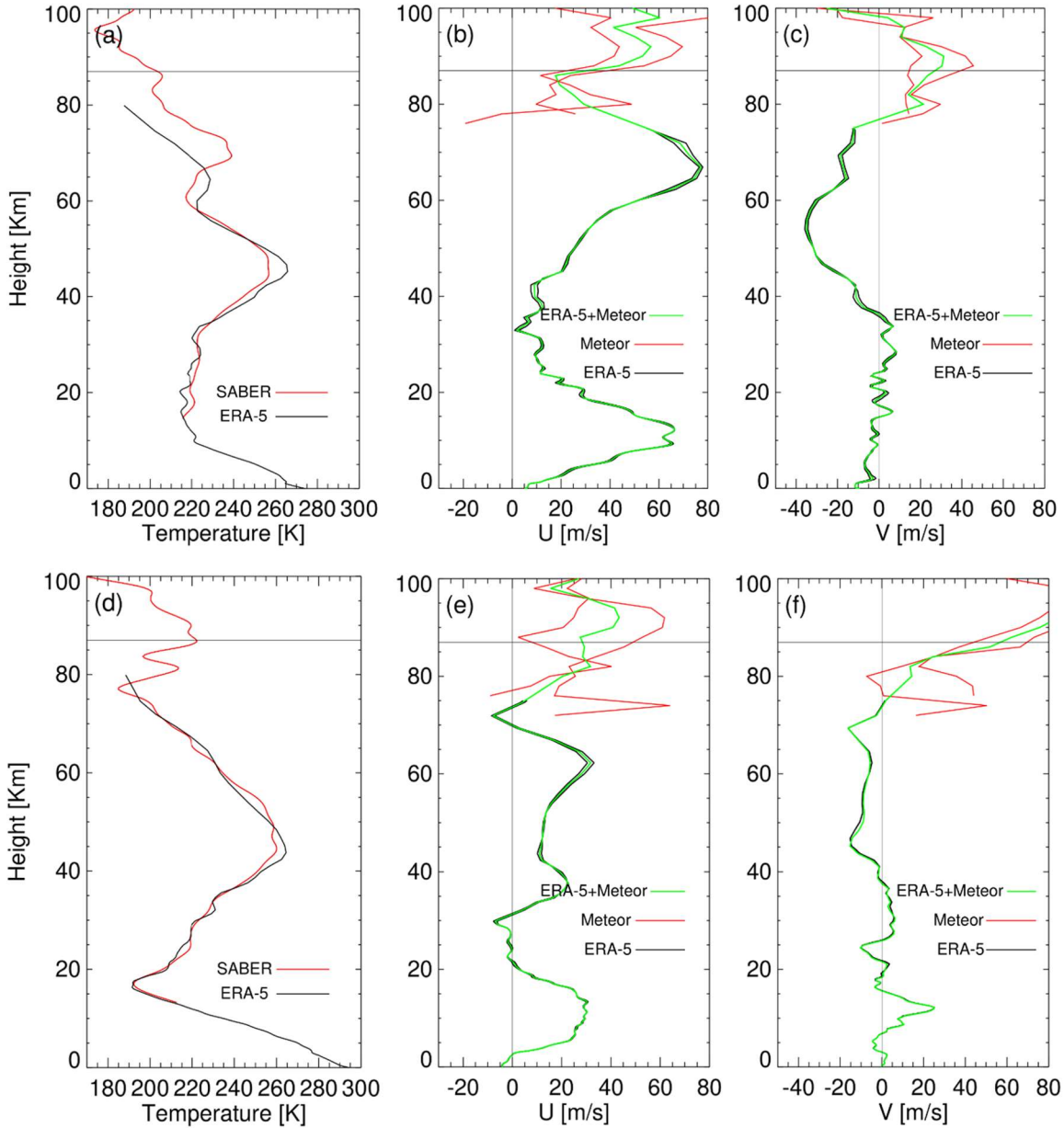
394  
 395 **Figure 11** (a) Backward ray tracing results of the wave packet #3 observed by the OH airglow network.  
 396 The red triangles and red crosses represent the trace start and termination points, respectively. (b)  
 397 Simulated tsunamis induced by the atmospheric pressure wave (TIAPW) corresponding to the dotted  
 398 rectangular area in (a). (c) Ray paths of the wave starting from the seven sampling points in (a).

399 According to the theory of AGW dispersion, the AGW propagating obliquely has  
 400 the following approximate relationship:  $\sin(\varphi) \sim T_b/T$ ,  $\varphi$  is the oblique propagation  
 401 angle,  $T_b$  is the buoyancy period,  $T$  is the intrinsic period. Azeem et al. (2007) found that  
 402 the disturbances in the ionosphere excited by the 2011 Tohoku tsunamis when they reached  
 403 the west coast of the United States. They concluded that the fluctuations observed in TEC  
 404 satisfy AGW dispersion relation, and the period and horizontal wavelength of the TEC

405 disturbances increased with distance from the West Coast of the U.S.

406 From the airglow network observations, we found that the wave packets #4-5 excited  
407 by the tsunamis, continues to propagate over the main land more than 3000 km from the  
408 coast. If the AGWs observed by the airglow network propagate freely rather than being  
409 constrained by duct, we will obtain the propagation characteristics similar to that observed  
410 by Azeem et al. (2007) in the ionosphere from TEC observations.  $T_p$  is about 5min from  
411 the SABER/TIMED observation. The period of wave packet #3 is between 5.5 min and 8.5  
412 min. The minimum propagation angle  $\varphi$  equals  $35^\circ$ , and the corresponding maximum  
413 propagation distance  $L$  is 125 km from  $L \sim H_{oh}/\tan(\varphi)$  estimation, where  $H_{oh}=87$  km is the  
414 height of OH airglow layer. However, our observation does not satisfy the free oblique  
415 propagation dispersion theory of AGWs. In addition, we did not find that the GW  
416 horizontal wavelength increased with the distance from the shore, as predicted by the  
417 theory of AGW oblique propagation. Therefore, the AGWs excited by the tsunami we  
418 observed in the mesopause region may be modulated by duct.

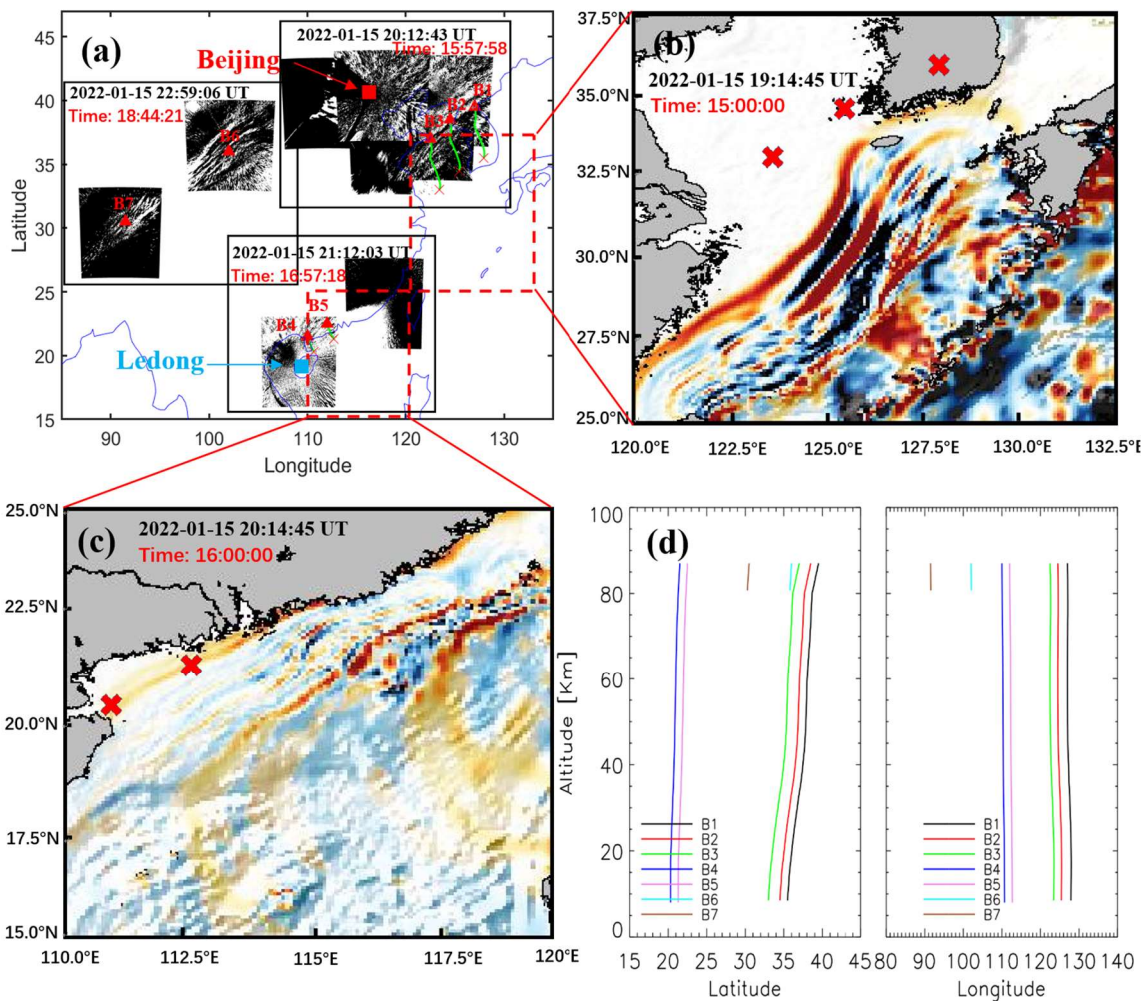
419 We did find a duct structure between 80 and 93 km (black solid line in Fig. 9b), while  
420 the wave packet #3 were in a state of free propagation when they propagate around the  
421 coastal vicinity of Chinese Mainland (dotted line and dashed line). The duct almost includes  
422 the whole OH airglow layer. Therefore, we believe that AGWs generated by TITVE may  
423 enter the duct in the process of propagation over Chinese Mainland. The duct structure over  
424 Chinese Mainland can explain that the GWs generated by the tsunamis can propagate  
425 thousands of kilometers inland.



426  
 427 **Figure 12** Similar for Figure 10, but for ray tracing analysis for the TITVE events. The SABER  
 428 temperature field in (a) comes from ascending track #1(21:17:50 UT, 21:18:33UT, 21:19:43 UT, and  
 429 21:20:43 UT) in Fig. 9, and the meteor radar wind fields in (b) and (c) come from Beijing station. The  
 430 SABER temperature field in (d) is from ascending track #1(21:12:51 UT, 21:14:01 UT, and 21:14:44  
 431 UT) in Fig. 9, and the meteor radar wind fields in (e) and (f) are from Ledong station.  
 432

433 Figure 13 shows the results of ray tracing for wave packets #4-5. The background field  
 434 used for ray tracing analysis for the wave packets #4-5 is from Fig. 12. Meteor radar wind  
 435 field is from Ledong station (18.3°N, 109.4°E). The horizontal wavelength of wave packets  
 436 #4 and #5 observed near the coast by the OH airglow network approximately  $89 \text{ km} \pm 6 \text{ km}$

437 and  $80 \text{ km} \pm 4 \text{ km}$ . We find that the source location of AGWs over the coast of Chinese  
 438 Mainland falls in the near tsunami area, while the location of AGW ray termination over  
 439 the inland is around  $80 \text{ km}$  (position B6 and B7 in Fig. 13d), which indicates that the wave  
 440 meets the evanescent layer (Wrasse et al., 2006). This is consistent with the duct structure  
 441 obtained through dispersion relation. Therefore, we suggest that TITVE interact with the  
 442 atmosphere after arriving at the coast of Chinese Mainland to generate the upward  
 443 propagating AGW packet. After reaching the mesopause region, this wave packet enters the  
 444 wave duct structure in the horizontal propagation process, and this wave duct supports  
 445 wave packet #5 to propagate more than  $3000 \text{ km}$  inland China.



446  
 447 **Figure 13** (a) Backward ray tracing results of the fourth and fifth group GWs observed by the OH airglow

448 network. The red triangles and red crosses represent the trace start and termination points, respectively. (b)  
449 and (c) Simulated tsunami directly induced by the Tonga volcano eruption (TITVE) corresponding to the  
450 dotted rectangular area in (a). (c) Ray paths of the wave starting from the seven sampling points in (a).

#### 451 **4. Conclusions**

452 Strong atmospheric disturbances, including Lamb waves, acoustic waves, and gravity  
453 waves, were triggered by the 2022 HTHH volcano eruption. The HTHH submarine  
454 volcanic eruption also triggered an unusual tsunami, which can generate atmospheric  
455 gravity waves (Fig. 14). We observed five strong group atmospheric waves associated with  
456 the HTHH volcano eruption from the ground-based airglow network observations.

457 The phase speed of the wave packet #1 is approximately 309 m/s, which is observed  
458 almost simultaneously with the surface Lamb wave L0 mode. Wave packet #2, with  
459 average phase speed of 236 m/s, has been confirmed as Lamb wave L1 mode from  
460 theoretical prediction. Wave packet # 3 and wave packets #4-5 are generated by TIAPW  
461 and TITVE from backward ray tracing analysis. The horizontal phase speed distribution  
462 range of wave packets #3-5 is 200 m/s to 215 m/s, which is smaller than that of wave  
463 packets # 1-2. For amplitude, the average amplitude of the lamb wave L1 mode (5.4%) is  
464 higher than that of the lamb wave L0 mode (3.2%), while wavepacket # 3, # 4, and # 5  
465 have relatively small amplitudes, mainly distributed between 0.85% and 1.25%. The  
466 horizontal wavelengths of the atmospheric AGWs observed by the airglow network are  
467 very consistent with those of the tsunami near the coast. This is the first time that we  
468 observed the AGWs in the mesopause region triggered by the tsunamis using optical  
469 detection equipment. It is also the first time to report atmospheric gravity waves excited by  
470 TIAPW.

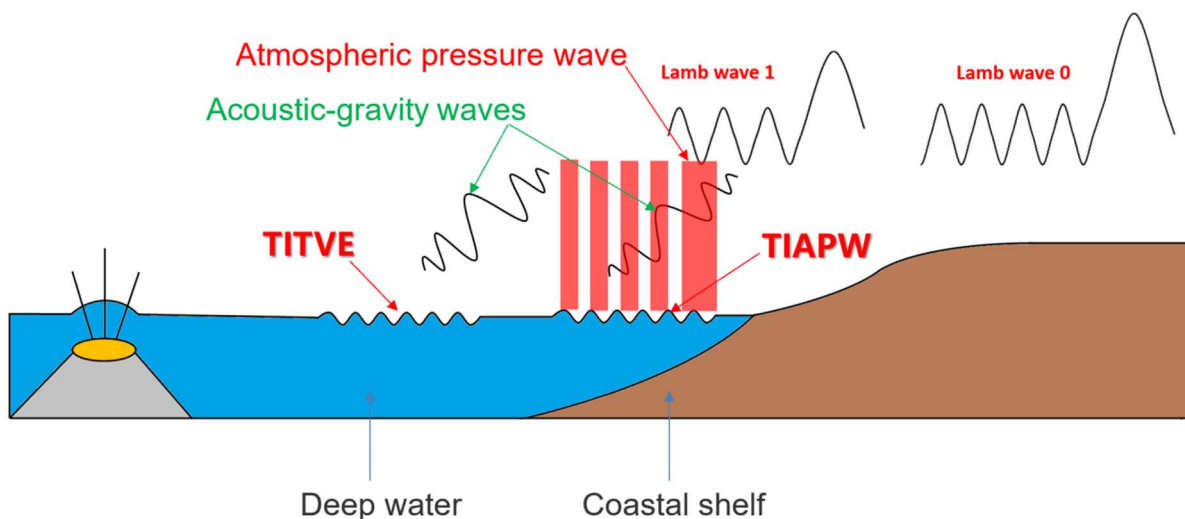
471 When the wave excited by TITVE propagate far away from the coast, the  
472 characteristics of AGWs are not consistent with the dispersion of free propagation AGWs.  
473 We find these wave packets are controlled by the duct, which can support the propagation  
474 of these GWs for thousands of kilometers after the tsunami were stopped at the coast.  
475 Therefore, tsunamis can have a significant impact on the upper atmosphere over inland  
476 areas far from the ocean through AGWs.

477 The 2022 HTHH volcano eruption form a complex coupling relationship in the land-  
478 ocean-atmosphere system (Fig. 14). Firstly, the heat released by the eruption has a direct  
479 impact on the ocean, causing temperature changes in the surrounding waters. This can lead  
480 to changes in the marine environment, affecting the behavior, distribution, and ecosystem  
481 structure of organisms.

482 Meanwhile, volcanoes release gases such as carbon dioxide and sulfur dioxide.  
483 Carbon dioxide is one of the greenhouse gases that can cause an increase in Earth's  
484 temperature, leading to global warming. Sulfur dioxide can cause sulfuric acid mist in the  
485 atmosphere, which affects the reflectivity and temperature of the atmosphere, and thus  
486 affects the global climate.

487 Moreover, the 2022 HTHH volcano eruptions also trigger atmospheric waves and  
488 tsunamis. The surface atmospheric pressure wave generated by the 2022 HTHH volcano  
489 eruption can affect the upper atmosphere. The conventional tsunami triggered by the Tonga  
490 volcano generated AGWs. The atmospheric pressure wave from the eruption generated a  
491 fast tsunami never before observed by tsunami observation networks. When the tsunamis  
492 reach the coast, their speeds decrease but their amplitudes increase, and the AGWs

493 generated by them will also affect the upper atmosphere. These AGWs play an important  
 494 coupling role between the ocean and the atmosphere by affecting the density and pressure  
 495 distribution of the atmosphere during propagation, leading to changes in the wind field and  
 496 affecting global atmospheric circulation. This study exhibits special dynamic coupling  
 497 process between air and sea via acoustic gravity waves (Fig. 14). This indirect impact on  
 498 the upper atmosphere provides a new perspective for us to study the coupling between the  
 499 ocean and the atmosphere and a key opportunity to improve the air-sea coupling model,  
 500 thereby enhancing our future ability to make tsunami warning forecasts.



501  
 502 **Figure 14** The Tonga volcano eruptions triggered two types of tsunamis, one type of tsunami is induced  
 503 by the atmospheric pressure wave (TIAPW) and the other type tsunami is directly induced by the Tonga  
 504 volcano eruption (TITVE). The acoustic gravity waves (AGWs) caused by tsunamis can propagate to the  
 505 mesopause region.  
 506

507 **Data availability**

508 The Multi-Layer Airglow Network data is available  
 509 at <https://data2.meridianproject.ac.cn/data> (MPDC, 2024). TIMED/SABER data is accessed  
 510 from <http://saber.gats-inc.com/data.php> (last access: 10 January 2024). The ERA5 reanalysis  
 511 data are able to be downloaded from the Copernicus Climate Change Service Climate Data



512 Store through <https://www.ecmwf.int/en/forecasts/datasets/reanalysis-datasets/era5> (last  
513 access: 12 January 2024). Himawari-8 data are distributed by the Center for Environmental  
514 Remote Sensing ([http://www.cr.chiba-u.jp/databases/GEO/H8\\_9/FD/index\\_en\\_V20190123.](http://www.cr.chiba-u.jp/databases/GEO/H8_9/FD/index_en_V20190123.html)  
515 html) (last access: 20 January 2024).

516

### 517 **Video supplements**

518 Multi-group of strong atmospheric waves observed over China associated with the 2022  
519 Hunga Tonga–Hunga Ha’apai volcano eruptions (<https://doi.org/10.5446/66190> Li, 2024).  
520 Animation series of OH airglow disturbances associated with the 2022 Hunga  
521 Tonga–Hunga Ha’apai volcano eruptions ([https://doi.org/10.5446/s\\_1689](https://doi.org/10.5446/s_1689) Li, 2024). A  
522 strong wave front observed by an OI 630 nm airglow imager over China associated with the  
523 2022 Hunga Tonga–Hunga Ha’apai volcano eruptions (<https://doi.org/10.5446/66280> Li,  
524 2024).

525

### 526 **Author contributions**

527 J.X and Q.L. conceived the idea of the manuscript. Q.L. carried out the data analysis,  
528 interpretation and manuscript preparation. A.R.G. developed and performed the numerical  
529 simulations. W.L and Y.Z compiled, processed and analysed satellite data. H.L.L., X.L,  
530 and W.Y. contributed to the data interpretation and manuscript preparation. All authors  
531 discussed the results and commented on the manuscript.

532

### 533 **Competing interests**

534 The authors declare no competing interests.

535

## 536 **Acknowledgements**

537 This work was supported by the National Science Foundation of China (42374205,  
538 41831073, and 41974179). The project is also supported by the Specialized Research Fund  
539 for State Key Laboratories. We acknowledge the use of data from the Chinese Meridian  
540 Project.

541

## 542 **References**

543 Adam, D.: Tonga volcano eruption created puzzling ripples in Earth's atmosphere, *Nature*,  
544 601, 497, <https://www.nature.com/articles/d41586-022-00127-1>, 2022.

545 Amores, A., Monserrat, S., Marcos, M., Argüeso, D., Villalonga, J., Jordà, G., and Gomis,  
546 D.: Numerical simulation of atmospheric Lamb waves generated by the 2022  
547 Hunga-Tonga volcanic eruption, *Geophysical Research Letters*, 49,  
548 <https://doi.org/10.1029/2022GL098240>, 2022.

549 Astafyeva, E., Maletckii, B., Mikesell, T. D., Munaibari, E., Ravanelli, M., Coisson, P., et al.  
550 The 15 January 2022 Hunga Tonga eruption history as inferred from ionospheric  
551 observations, *Geophysical Research Letters*, 49,  
552 <https://doi.org/10.1029/2022GL098827>, 2022.

553 Azeem, I., Vadas, S. L., Crowley, G., and Makela, J. J.: Traveling ionospheric disturbances  
554 over the United States induced by gravity waves from the 2011Tohoku tsunami and  
555 comparison with gravity wave dissipative theory, *J. Geophys. Res. Space Physics*, 122,

556 3430–3447, <https://doi.org/10.1002/2016JA023659>, 2017.

557 Beer, T. *Atmospheric Waves*, 300 pp., John Wiley, New York, 1974.

558 Carvajal, M., Sepúlveda, I., Gubler, A., and Garreaud, R.: Worldwide signature of the 2022  
559 Tonga volcanic tsunami, *Geophysical Research Letters*, 49(6),  
560 <https://doi.org/10.1029/2022GL098153>, 2022.

561 Donn, W. L., and Balachandran, N. K.: Mount St. Helens eruption of 18 May 1980: Air  
562 waves and explosive yield, *Science* 213, 539 – 541,  
563 <https://doi.org/10.1126/science.213.4507.539>, 1981.

564 Duncombe, J.: The surprising reach of Tonga’s Giant atmospheric waves, *Eos*, 103, 2022.

565 Duncombe, J.: The surprising reach of Tonga’s Giant atmospheric waves, *Eos*, 103,  
566 <https://doi.org/10.1029/2022EO220050>, 2022.

567 Francis, S. H.: Acoustic-gravity modes and large-scale traveling ionospheric disturbances of  
568 a realistic, dissipative atmosphere, *J. Geophys. Res.*, 78 (13), 2278–2301,  
569 <https://doi.org/10.1029/JA078i013p02278>, 1973.

570 Garcia, F. J., Taylor, M. J., and Kelley, M. C.: Two-dimensional spectral analysis of  
571 mesospheric airglow image data, *Appl. Optics*, 36 (29), 7374–7385,  
572 <https://doi.org/10.1364/AO.36.007374>, 1997.

573 Ghent, J. N., and Crowell, B. W.: Spectral characteristics of ionospheric disturbances over  
574 the southwestern Pacific from the 15 January 2022 Tonga eruption and tsunami,  
575 *Geophysical Research Letters*, 49, <https://doi.org/10.1029/2022GL100145>, 2022.

576 Gossard, E. E., and Hooke, W. H.: *Waves in the Atmosphere*, Elsevier, Amsterdam, 1975,  
577 456.

578 Grawe, M. A., and Makela, J. J.: The ionospheric responses to the 2011 Tohoku, 2012

579 Haida Gwaii, and 2010 Chile tsunamis: Effects of tsunami orientation and observation  
580 geometry, *Earth and Space Science*, 2, 472–483,  
581 <https://doi.org/10.1002/2015EA000132>, 2015.

582 Grawe, M. A., and Makela, J. J.: Observation of tsunami-generated ionospheric signatures  
583 over Hawaii caused by the 16 September 2015 Illapel earthquake, *J. Geophys. Res.*  
584 *Space Physics*, 122, 1128–1136, <https://doi.org/10.1002/2016JA023228>, 2017.

585 Gusman, A.R., Roger, J., Noble, C. et al. The 2022 Hunga Tonga-Hunga Ha’apai Volcano  
586 Air-Wave Generated Tsunami, *Pure and Applied Geophysics*, 179, 3511–3525,  
587 <https://doi.org/10.1007/s00024-022-03154-1>, 2022.

588 Harkrider, D., and Press, F.: The Krakatoa air-sea waves: An example of pulse propagation  
589 in coupled systems, *Geophys. J. R. Astron. Soc.* 13, 149 – 159,  
590 <https://doi.org/10.1111/j.1365-246X.1967.tb02150.x>, 1967.

591 Hersbach, H., Bell, B., Berrisford, P., Hirahara, S., Horányi, A., Muñoz-Sabater, J., Nicolas,  
592 J., Peubey, C., Radu, R., Schepers, D., Simmons, A., Soci, C., Abdalla, S., Abellan, X.,  
593 Balsamo, G., Bechtold, P., Biavati, G., Bidlot, J., Bonavita, M., De Chiara, G.,  
594 Dahlgren, P., Dee, D., Diamantakis, M., Dragani, R., Flemming, J., Forbes, R.,  
595 Fuentes, M., Geer, A., Haimberger, L., Healy, S., Hogan, R. J., Hólm, E., Janisková,  
596 M., Keeley, S., Laloyaux, P., Lopez, P., Lupu, C., Radnoti, G., deRosnay, P., Rozum,  
597 I., Vamborg, F., Villaume, S., and Thépaut, J. N. The ERA5 global reanalysis, *Q. J. R.*  
598 *Meteorol. Soc.*, 146, 1999–2049, <https://doi.org/10.1002/qj.3803>, 2020 (data available  
599 at: <https://www.ecmwf.int/en/forecasts/datasets/reanalysis-datasets/era5> last access: 12  
600 January 2024).

601 Hickey, M. P., Schubert, G., and Walterscheid, R. L.: Propagation of tsunami-driven  
602 gravity waves into the thermosphere and ionosphere, *J. Geophys. Res.*, 114,  
603 <https://doi.org/10.1029/2009JA014105>, 2009.

604 Hickey, M. P., Schubert, G., and Walterscheid, R. L.: Atmospheric airglow fluctuations due  
605 to a tsunami-driven gravity wave disturbance, *Journal of Geophysical Research*,  
606 115(A6), A06308, <https://doi.org/10.1029/2009JA014977>, 2010.

607 Hines, C.: Gravity waves in the atmosphere, *Nature*, 239 (5367), 73–78,  
608 <https://doi.org/10.1038/239073A0>, 1972.

609 Inchin, P. A., Heale, C. J., Snively, J. B., and Zettergren, M. D.: The dynamics of nonlinear  
610 atmospheric acoustic-gravity waves generated by tsunamis over realistic bathymetry,  
611 *Journal of Geophysical Research: Space Physics*, 125,  
612 <https://doi.org/10.1029/2020JA028309>, 2020.

613 Inchin, P. A., Heale, C. J., Snively, J. B., and Zettergren, M.D.: Numerical modeling of  
614 tsunami-generated acoustic-gravity waves in mesopause airglow, *Journal of*  
615 *Geophysical Research: Space Physics*, 127, <https://doi.org/10.1029/2022JA030301>,  
616 2022.

617 Koketsu K. and Higashi S.: Three-dimensional topography of the sediment/basement  
618 interface in the Tokyo Metropolitan area, Central Japan, *Bull. seism. Soc. Am.*, 82,  
619 2328-2349, <https://doi.org/10.1785/BSSA0820062328>, 1992.

620 Kubota, T., Saito, T., & Nishida, K.: Global fast-traveling tsunamis driven by atmospheric  
621 Lamb waves on the 2022 Tonga eruption, *Science*, 377, 91-94,  
622 <https://doi.org/10.1126/science.abo4364>, 2022.

623 Laughman, B., Fritts, D. C., and Lund, T. S.: Tsunami-driven gravity waves in the presence  
624 of vertically varying background and tidal wind structures, *J. Geophys. Res. Atmos.*,  
625 122, 5076-5096, <https://doi.org/10.1002/2016JD025673>, 2017.

626 Li, X., Ding, F., Yue, X., Mao, T., Xiong, B., and Song, Q.: Multiwave structure of  
627 traveling ionospheric disturbances excited by the Tonga volcanic eruptions observed  
628 by a dense GNSS network in China, *Space Weather*, 21,  
629 <https://doi.org/10.1029/2022SW003210>, 2023.

630 Lighthill, M. J.: *Waves in Fluids*, Cambridge University Press, Cambridge, UK, New York,  
631 504 pp., ISBN: 0-521-01045-4, 1978.

632 Lin, J.-T., Rajesh, P. K., Lin, C. C. H., Chou, M.-Y., Liu, J.-Y., Yue, J., et al. Rapid  
633 conjugate appearance of the giant ionospheric Lamb wave signatures in the northern  
634 hemisphere after Hunga-Tonga volcano eruptions, *Geophysical Research Letters*, 49,  
635 <https://doi.org/10.1029/2022GL098222>, 2022.

636 Lindzen, R. S., and Blake, D.: Lamb waves in the presence of realistic distributions of  
637 temperature and dissipation, *Journal of Geophysical Research*, 77(12), 2166 – 2176,  
638 <https://doi.org/10.1029/JC077i012p02166>, 1972.

639 Li, Q., Xu, J., Liu, H., Liu, X., and Yuan, W.: How do gravity waves triggered by a typhoon  
640 propagate from the troposphere to the upper atmosphere?. *Atmos. Chem. Phys.*, 22,  
641 12077–12091, <https://doi.org/10.5194/acp-22-12077-2022>, 2022.

642 Li, Q.: Multi-group of strong atmospheric waves observed over China associated with the  
643 2022 Hunga Tonga–Hunga Ha’apai volcano eruptions, TIB AV-Portal [video],  
644 <https://doi.org/10.5446/66190>, 2024.

645 Li, Q.: Animation series of OH airglow disturbances associated with the 2022 Hunga  
646 Tonga–Hunga Ha’apai volcano eruptions, TIB AV-Portal [video],  
647 [https://doi.org/10.5446/s\\_1689](https://doi.org/10.5446/s_1689), 2024. Li, Q.: A strong wave front observed by an OI 630  
648 nm airglow imager over China associated with the 2022 Hunga Tonga–Hunga Ha’apai  
649 volcano eruptions, TIB AV-Portal [video], <https://doi.org/10.5446/66280>, 2024.

650 Liu, H.-L., Wang, W., Huba, J.D., Lauritzen, P. H., and Vitt, F. Atmospheric and  
651 Ionospheric Responses to Hunga-Tonga Volcano Eruption Simulated by WACCM-X,  
652 Geophysical Research Letters, 50, <https://doi.org/10.1029/2023GL103682>, 2023.

653 Liu, X., Xu, J., Yue, J., and Kogure, M.: Strong gravity waves associated with Tonga  
654 volcano eruption revealed by SABER observations, Geophysical Research Letters, 49,  
655 <https://doi.org/10.1029/2022GL098339>, 2022.

656 Makela, J. J., Lognonné, P., Hébert, H., Gehrels, T., Rolland, L., Allgeyer, S., et al. Imaging  
657 and modeling the ionospheric airglow response over Hawaii to the tsunami generated by  
658 the Tohoku earthquake of 11 March 2011, Geophysical Research Letters, 38 (24),  
659 <https://doi.org/10.1029/2011GL047860>, 2011.

660 MPDC: Airglow data [data set], <https://data2.meridianproject.ac.cn/data>, last access: 15  
661 January 2024.

662 Nishikawa, Y., Yamamoto, My., Nakajima, K. et al. Observation and simulation of  
663 atmospheric gravity waves exciting subsequent tsunami along the coastline of Japan  
664 after Tonga explosion event, Sci Rep 12, 22354, <https://doi.org/10.1038/s41598-022-25854-3>, 2022.

666 Occhipinti, G., Rolland, L., Lognonné, P., and Watada, S.: From Sumatra 2004 to

667 Tohoku-Oki 2011: The systematic GPS detection of the ionospheric signature induced  
668 by tsunamigenic earthquakes, *Journal of Geophysical Research: Space Physics*, 118,  
669 3626–3636, <https://doi.org/10.1002/jgra.50322>, 2013.

670 Omira, R., Ramalho, R.S., Kim, J. et al. Global Tonga tsunami explained by a fast-moving  
671 atmospheric source, *Nature* 609, 734–740, [https://doi.org/10.1038/s41586-](https://doi.org/10.1038/s41586-022-04926-4)  
672 022-04926-4, 2022.

673 Otsuka, S.: Visualizing Lamb waves from a volcanic eruption using meteorological satellite  
674 Himawari-8. *Geophysical Research Letters*, 49, [https://doi.org/10.1029/](https://doi.org/10.1029/2022GL098324)  
675 2022GL098324, 2022 (data available at: [http://www.cr.chiba-u.jp/databases/GEO/](http://www.cr.chiba-u.jp/databases/GEO/H8_9/FD/index_en_V20190123.html)  
676 H8\_9/FD/index\_en\_V20190123.html last access: 20 January 2024).

677 Peltier, W., and Hines, C.: On the possible detection of tsunamis by a monitoring of the  
678 ionosphere, *Journal of Geophysical Research*, 81(12), 1995–2000,  
679 <https://doi.org/10.1029/JC081i012p01995>, 1976.

680 Poblet, F. L., Chau, J. L., Conte, J. F., Vierinen, J., Suclupe, J., Liu, A., and Rodriguez, R. R.:  
681 Extreme horizontal wind perturbations in the mesosphere and lower thermosphere over  
682 South America associated with the 2022 Hunga eruption, *Geophysical Research Letters*,  
683 50, <https://doi.org/10.1029/2023GL103809>, 2023.

684 Pradipta, R., Carter, B. A., Currie, J. L., Choy, S., Wilkinson, P., Maher, P., and Marshall, R.:  
685 On the propagation of traveling ionospheric disturbances from the Hunga Tonga-Hunga  
686 Ha'apai volcano eruption and their possible connection with tsunami waves,  
687 *Geophysical Research Letters*, 50, <https://doi.org/10.1029/2022GL101925>, 2023.

688 Press, F., and Harkrider, D. G.: “Propagation of acoustic-gravity waves in the atmosphere,” *J.*



689 Geophys. Res. 67, 3889–3908, 1962.doi:10.1029/JZ067i010p03889.

690 Salmon, R.: Introduction to ocean waves, Scripps Inst. of Oceanogr., Univ. of Calif., San  
691 Diego., 2014.

692 Sepúlveda, I., Carvajal, M., and Agnew, D. C.: Global winds shape planetary-scale Lamb  
693 waves. *Geophysical Research Letters*, 50, <https://doi.org/10.1029/2023GL106097>,  
694 2023

695 Smith, S.M., Martinis, C. R., Baumgardner, J., and Mendillo, M.: All-sky imaging of  
696 transglobal thermospheric gravity waves generated by the March 2011 Tohoku  
697 Earthquake, *J. Geophys. Res. Space Physics*, 120, 10,992–10,999,  
698 <https://doi.org/10.1002/2015JA021638>, 2015.

699 Swenson, G. R. and Mende, S. B.: OH emission and gravity waves (including a breaking  
700 wave) in all-sky imagery from Bear Lake, UT, *Geophys. Res. Lett.*, 21, 2239–2242,  
701 <https://doi.org/10.1029/94GL02112>, 1994.

702 Symons, G. J.: The Eruption of Krakatoa, and Subsequent Phenomena: Report of the  
703 Krakatoa Committee of the Royal Society (Wiley Online Library), 1888.

704 Takahashi, H., Figueiredo, C.A.O.B., Barros, D. et al. Ionospheric disturbances over South  
705 America related to Tonga volcanic eruption, *Earth Planets Space* 75, 92,  
706 <https://doi.org/10.1186/s40623-023-01844-1>, 2023.

707 Tang, J., Kamalabadi, F., Franke, S. J., Liu, A. Z., and Swenson, G. R.: Estimation of gravity  
708 wave momentum flux with spectroscopic imaging, *IEEE T. Geosci. Remote*, 43,  
709 103–109, <https://doi.org/10.1109/TGRS.2004.836268>, 2005.

710 Themens, D. R., Watson, C., Zagar, N., Vasylykevych, S., Elvidge, S., McCaffrey, A., et al.

711 Global propagation of ionospheric disturbances associated with the 2022 Tonga  
712 volcanic eruption, *Geophysical Research Letters*, 49(7),  
713 <https://doi.org/10.1029/2022GL098158>, 2022.

714 Vadas, S. L., Makela, J. J., Nicolls, M. J., and Milliff, R. F.: Excitation of gravity waves by  
715 ocean surface wave packets: Upward propagation and reconstruction of the  
716 thermospheric gravity wave field, *J. Geophys. Res. Space Physics*, 120, 9748–9780,  
717 <https://doi.org/10.1002/2015JA021430>, 2015.

718 Xu, J., Li, Q., Sun, L., Liu, X., Yuan, W., Wang, W., Yue, J., Zhang, S., Liu, W., Jiang, G.,  
719 Wu, K., Gao, H., and Lai, C.: The Ground - Based Airglow Imager Network in China:  
720 Recent Observational Results, *Geophysical Monograph Series*, 261, 365-394,  
721 <https://doi.org/10.1002/9781119815631.ch19>, 2021.

722 Xu, J., et al. Concentric gravity waves over northern China observed by an airglow imager  
723 network and satellites, *J. Geophys. Res. Atmos.*, 120, 11,058–11,078,  
724 <https://doi.org/10.1002/2015JD023786>, 2015.

725 Yamada, M., Ho, T.-C., Mori, J., Nishikawa, Y., and Yamamoto, M.-Y.: Tsunami triggered  
726 by the Lamb wave from the 2022 Tonga volcanic eruption and transition in the  
727 offshore Japan region, *Geophysical Research Letters*, 49,  
728 <https://doi.org/10.1029/2022GL098752>, 2022.

729 Yeh, K. C., and Liu, C. H.: Acoustic-Gravity Waves in the Upper Atmosphere, *Reviews of*  
730 *Geophysics and Space Physics*, 12 (2), 193, <https://doi.org/10.1029/RG012i002p00193>,  
731 1974.

732 Wrasse, C. M., Nakamura, T., Tsuda, T., Takahashi, H., Medeiros, A. F., Taylor, M.

733 J., Gobbi, D., Salatun, A., Suratno, E. A., and Admiranto, A. G.: Reverse ray tracing of  
734 the mesospheric gravity waves observed at 23°S (Brazil) and 7°S (Indonesia) in airglow  
735 imagers, *J. Atmos. Sol. Terr. Phys.*, 68, 163– 181,  
736 <https://doi.org/10.1016/j.jastp.2005.10.012>, 2006.

737 Wright, C.J., et al. Surface-to-space atmospheric waves from Hunga Tonga-Hunga Ha’apai  
738 eruption, *Nature*, 609 (7928), 741–746, <https://doi.org/10.1038/s41586-022-05012-5>,  
739 2022.

740 Zhang, S., Vierinen, J., Aa, E., Goncharenko, L. P., Erickson, P., Rideout, W., et al. 2022  
741 Tonga volcanic eruption induced global propagation of ionospheric disturbances via  
742 Lamb waves, *Frontiers in Astronomy and Space Sciences*, 9, 1–10,  
743 <https://doi.org/10.3389/fspas.2022.871275>, 2022.